# Discovery of a 150 day period in the Venus condensational clouds

Kevin McGouldrick [a,*], Constantine C.C. Tsang [b]

[a] Laboratory for Atmospheric and Space Physics, University of Colorado Boulder, 3665 Discovery Dr., Boulder, CO 80303, United States
[b] Southwest Research Institute, Department of Space Studies, 1050 Walnut St., Suite 300, Boulder, CO 80302, United States

## ABSTRACT

We have analyzed the long-term regional and global variation of emitted radiance in 1.74 µm and 2.30 µm near infrared spectral windows in the Venus atmosphere using the medium resolution, infrared channel of the Visible and Infrared Thermal Imaging Spectrometer (VIRTIS-M-IR) on the Venus Express spacecraft. We find a periodic variation in the 1.74 µm radiance that is most pronounced at mid-latitudes ($30° - 60°$ latitude). This oscillation has a period of approximately 150 days, and is shown to be unlikely to be driven by variations in viewing geometry, nor by variations in instrumental characteristics such as spectrometer temperature. The oscillation has an amplitude at least as large as that of the typical day-to-day variations observed. The decay and recovery timescales are consistent with response of the cloud vertical structure to the radiative-dynamical feedback. It remains unclear why this variation would be seen only at mid-latitudes, but some hypotheses to guide future modeling testing are suggested.

## 1. Introduction

Spatial and temporal inhomogeneities in the near infrared emission spectrum of Venus were first discovered by Allen and Crawford (1984). It was soon determined that these inhomogeneities were observed as a consequence of the existence of narrow spectral windows in the near infrared emission spectrum of Venus where absorption by (primarily) $CO_2$ and $H_2O$ was minimal. Since then, these spectral windows have been used to elucidate the properties of the surface of Venus (for example, Mueller et al. (2008), Kappel et al. (2012), Haus et al. (2014), and Shalygin et al. (2015)), atmospheric composition and chemistry (for example, Marcq et al. (2005) and Bézard et al. (2009)), and properties of the clouds of Venus (for example, Carlson et al. (1993) and Wilson et al. (2008)).

Crisp et al. (1989) and Kamp et al. (1988) showed that the variability of night side near infrared emission from Venus in the spectral vicinity of the 1.74 µm and 2.30 µm windows was driven primarily by variations in the condensational clouds of Venus. The clouds of Venus cover a range of altitudes from about 50 km above the surface to about 70 km above the surface. When viewed in emitted near infrared radiation, spatial inhomogeneities are driven by variations in the lower regions of the clouds, between about 50–55 km. The bulk of the cloud mass is located also in this region, but the origin of the volatiles that support the entire cloud system is the photochemically produced sulfuric acid around 63 km.

Grinspoon et al. (1993) used the 1.74 µm and 2.30 µm spectral windows observed by the Near Infrared Mapping Spectrometer (NIMS) during the *Galileo* flyby to constrain the total infrared optical depth of the photochemical and condensational clouds and the composition of the putative Mode 3 particles first postulated by Knollenberg and Hunten (1980). Carlson et al. (1993) used the same data to characterize the spatial variability of the typical size of the particles that comprise the condensational cloud at the time of the *Galileo* encounter.

More recently, the infrared mapping channel of the Visible and Infrared Thermal Mapping Spectrometer (VIRTIS-M-IR) on the *Venus Express* spacecraft (Drossart et al., 2007) has been utilized to further characterize the short-term evolution of the clouds of Venus (McGouldrick et al., 2012) and to simultaneously retrieve additional properties of the Venus clouds region, including cloud base altitude, sulfuric acid weight percent, and sub-cloud and in-cloud water vapor concentrations (Barstow et al., 2012).

Here, we build upon the work done in those two papers to characterize the long-term evolution of the clouds of Venus, as can be determined through analysis of 921 orbits (about two and a half years) of VIRTIS-M-IR observations of the night side of Venus.

* Corresponding author. Fax: +1 303 735 3737.
  E-mail addresses: kevin.mcgouldrick@lasp.colorado.edu, kevin.mcgouldrick@gmail.com (K. McGouldrick).

## 2. Observational data

*Venus Express* launched in November 2005, was placed into orbit around Venus in April 2006, and continued to return valuable science data until it exhausted the fuel for its attitude control thrusters in November 2014. Its polar orbit exhibited a periapsis altitude generally between 150 km and 250 km above the surface of Venus at about +80°latitude, and an apoapsis altitude of about 66,000 km. The VIRTIS-M infrared channel is a medium spatial resolution (0.25 mrad/pxl) infrared mapping spectrometer that covers the range of wavelengths from 1 µm to 5 µm with a spectral resolution of roughly $\lambda/\Delta\lambda \sim 300$, or about 0.01 µm. Though, in practice, the effective resolution has been shown to be about 0.017 µm (Bézard et al., 2009). This is sufficient spectral resolution to resolve many details of the spectral windows (Drossart et al., 2007). The spatial resolution is about 30 km when the spacecraft is at apoapse ($d \sim 66, 000$ km), improving to about 5 km at a distance of about 10, 000 km. The near infrared detector was a mercury-cadmium-telluride (HgCdTe) semiconductor cooled to 70 K. The instrument returned data over the course of nearly four sidereal Venus days until the cooling system failed during orbit 921 (UTC: 2008 October 27). The cooling system began to show signs of wear during the nominal mission (the first 500 orbits), so the frequency of use of the VIRTIS-M-IR instrument was significantly reduced between orbits 500 and 921, as compared with the nominal mission. Previous work by McGouldrick et al. (2012) exploring the long-term variability of the clouds relied on data only from the first 407 orbits of the mission. In the present work, we utilize the entire VIRTIS-M-IR data set.

The entire volume of data produced by the instrument can be obtained at the European Space Agency's (ESA's) Planetary Science Archive (PSA) website, and is mirrored by the National Astronautical and Space Administration's (NASA's) Planetary Data System (PDS), Atmospheres Node. The VIRTIS instrument produced about a terabyte of data over the course of the *Venus Express* mission. In order to efficiently analyze this large volume of data, it is necessary to filter it according to both instrumental and geometric constraints. Instrumentally, we consider only observations utilizing integration times of at least 0.3 s. Acquired spectral cubes having integration times shorter than this are intended for the much higher radiance from day side observations, and have very low signal to noise ratios in emitted near infrared light. Geometrically, we constrain the data according to distance, viewing angle, and solar angle considerations. To generate spectral cubes, VIRTIS-M-IR scans its slit across the field of view to generate spectral image cubes. The time required to do this, combined with the motion of the spacecraft relative to the planet, means that mapping mode spectral cubes generally are not created when within 10,000 km of the planet. (Drossart et al., 2007). Thus, we consider only data acquired at distances greater than 10, 000 km from the planet. In doing so, we are neglecting the pericenter observations – mostly of northern hemisphere targets. We choose to neglect these data for two reasons. First, these periapse observations are necessarily very parochial in nature, due to the small distance to Venus and the small field of view of VIRTIS-M-IR. While the inclusion of these nadir-viewing, near-periapse observations can improve the mission-long statistics, they also have the potential to introduce significant errors into the time series analysis performed in this work that are caused by the spatial inhomogeneity. Second, the present work is intended to be part of a larger project in which the information gathered here can inform the characterization of individual features, including morphology, in the Venus clouds over a variety of timescales. Since that effort will be necessarily limited to observations using the mapping mode of VIRTIS-M-IR, we also constrain this preliminary work to that mode of observation. The pericenter observations obtained at distances less than 10,000 km

will not be helpful in either of these contexts, so we disregard those observations for now in favor of concentrating on the southern hemisphere mapping data. We consider only those observations in which at least some of the night side is visible, discarding all data for which only the day side is seen. That is, we discard the data for the present analysis if the minimum hour angle of the Sun exceeds 5 a.m. and the maximum hour angle is less than 7 p.m. The 1 h buffer from the dawn or dusk terminator is intended to minimize the effects of sunlight that is forward scattered from beyond the terminator. We also restrict the observations to those that are affected minimally (or not at all) by sunlight that is forward scattered from the day side of the planet by restricting the data in the nominal analysis to locations where the solar incidence angle exceeds 95°. In order to quantify the effects of this cutoff, we also compare results considering a range of incidence angle, among 100°, 105°, 110°, and 115°. Note that, due to our hour angle restriction, these incidence angle data filters will have their greatest effect for observations near the pole. However, these cutoffs will have minimal effect on reducing the contribution by stray light sources in the data (Kappel et al., 2012). Finally, we restrict our analysis to the southern hemisphere. The highly eccentric polar orbit of *Venus Express* makes mapping type observations by VIRTIS-M-IR of the southern hemisphere more favorable than the northern hemisphere. While portions of the northern hemisphere have been observed in mapping mode, the data are almost exclusively equatorial ($|\phi| < 30°$). If a north-south hemispheric dichotomy exists in the behavior of the clouds then this uneven distribution of north and south latitudinal observations could exacerbate the effect. Furthermore, even those northern hemisphere observations that do exist are very close to the limb, and hence are subject to significant foreshortening and limb darkening, resulting in larger uncertainties in the corrected upwelling radiance.

Most of the time, at least some of the night side of Venus is visible to VIRTIS-M-IR. However, there are times when the change in the phase angle due to the revolution of Venus around the Sun, coupled with the telemetry requirements, makes it nearly impossible to observe the night side of the planet (which is necessary for the analysis of these near infrared emissions from Venus). Thus, even though VIRTIS-M-IR returned useful data over a window of 921 days (also 921 orbits, since the orbital period of *Venus Express* throughout this phase of the mission was 24 h) before the failure of its cooling system, there are somewhat fewer than 921 orbits' worth of data that will be useful for the present analysis. There are also several weeks-long breaks in the data during which times night side data that satisfy our declared criteria could not be obtained.

Over the course of multiple orbits, significant latitudinal and longitudinal coverage of the clouds in the southern hemisphere was built up, which allows for the determination of possible latitudinal tendencies in the existence and optical thickness of the clouds. Furthermore, VIRTIS observations sometimes utilize a mosaic mode in which the entire visible hemisphere of the planet is observed over the course of up to nine separate cube acquisitions. Observing in this manner allowed a greater spatial coverage than is possible with a single cube, or a series of cubes over a particular location.

Note that, due to the limited field of view of the VIRTIS-M-IR instrument, the brief lifetime of this instrument (fewer than four Venus sidereal days), and the existence of about a dozen unique science observation modes, the composite coverage of the planet is not homogeneous. In addition to the hemispherical observational imbalance driven by the polar and eccentric orbit, there may also be geographic locations that had been observed more frequently than others.

The VIRTIS-M cubes demonstrate a significant amount of anomalous radiance that has been attributed to scattered sunlight,
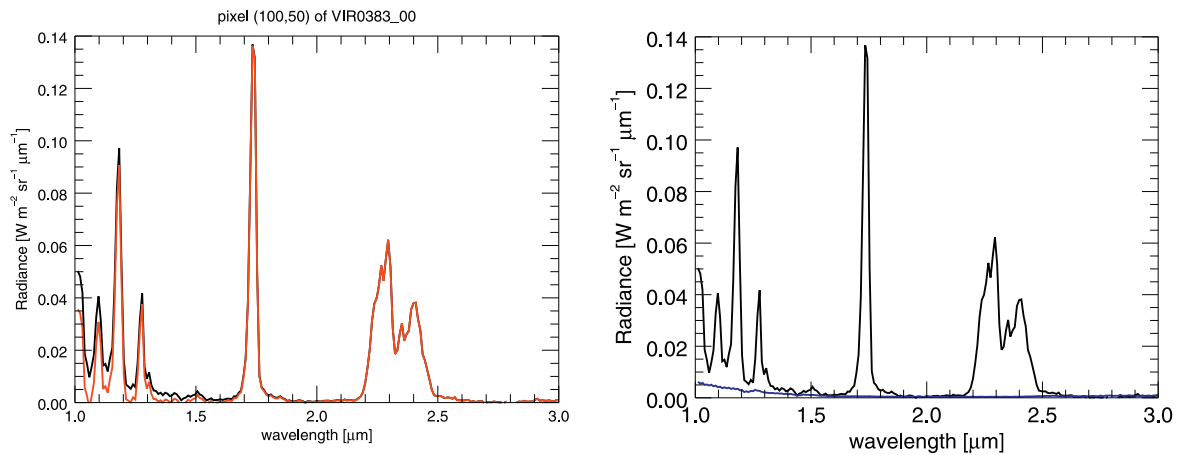
**Fig. 1.** In the left hand plot, the black curve is the uncorrected spectrum of sample 100 and line 50 of pure night side cube VIR0383_00. The red curve is the same data with the stray sunlight correction from Eq. (3) applied. In the right hand plot, an average spectrum collected from the empty space observations within the same image cube is compared with the same on-target uncorrected spectrum.

probably reflected from the baffle toward the detector (Kappel et al., 2012; Mueller et al., 2008). In order to correct for this scattered sunlight, we choose a series of wavelength bands in the Venus emitted near infrared spectrum for which we expect to see zero emitted radiance, due to the absorption of upwelling radiation by atmospheric constituents such as $CO_2$ and $H_2O$. That is, we define a series of "muntins[1]" between the near infrared spectral windows with wavelengths: ($1.05 \pm 0.01\,\mu m$, $1.225 \pm 0.015\,\mu m$, $1.38 \pm 0.03\,\mu m$, $1.57 \pm 0.03\,\mu m$). A VIRTIS image cube is a three-dimensional data construct with dimensions termed band (wavelength), sample (pixels along the slit), and line (each new integration by the detector). That is, a VIRTIS cube is a stack of *band* × *sample* images. For each *band* × *sample* image, we average over the sample (slit) dimension to find an average spectrum.

Acting on the assumption that the stray light was likely scattered sunlight, we had first attempted to fit the data in the muntins according to a reflected solar Blackbody curve:

$$I(\lambda) = A \frac{2hc^2}{\lambda^5} \left( e^{\frac{hc}{\lambda kT}} - 1 \right)^{-1} \qquad (1)$$

where $h$ is Planck's Constant, $c$ is the speed of light in vacuum, $k$ is Boltzmann's constant, $T$ is the temperature of the solar photosphere, and we choose $A$ to be an arbitrary gray albedo that is a free parameter to be fit to the data along with $\lambda$. However, we found that such a spectrum could not match the measured muntins. If the gray albedo was chosen to fit the muntins near 1.5 µm and 2.0 µm, then the stray light radiance from the muntins at shorter wavelengths was underestimated. Similarly, if the curve was fitted to the muntins at wavelengths shorter than 1.3 µm, then the stray light radiance from the longer wavelength muntins was overestimated. Similar to Kappel et al. (2012) and Longobardo et al. (2012), we found that the stray light radiance in the muntins closely matched a $\lambda^{-4}$ curve. Likely interpretations of such a curve would mean that either the source of the stray light spectrum were a blackbody considerably hotter than the Sun or was produced by a non-gray albedo that increased strongly at shorter wavelengths. In the former case, these near infrared wavelengths are too near the peak of the solar spectrum to be in the long-wavelength Rayleigh-Jeans regime of the solar spectrum that asymptotes to a $\lambda^{-4}$ curve. In the latter case, Kappel et al. (2012) suggest that the stray light resembles $\lambda^{-4}$ associated with

scattering processes, but the Venus cloud particles are too large to be Rayleigh scatterers at these wavelengths. Since neither of these explanations is likely, we chose to fit the data with an arbitrary power law or an arbitrary exponential:

$$I(\lambda) = I_0 \lambda^a \qquad (2)$$

$$I(\lambda) = I_0 \cdot e^{a\lambda} \qquad (3)$$

We then fit the free parameters ($I_0$) and ($a$) to the muntin data, finding their best fit values and standard deviations in each of these two cases. We found that the power law tended to identify best fit exponents of between $\lambda^{-3}$ and $\lambda^{-5}$, somewhat consistent with previous suggestions by Kappel et al. (2012) and Longobardo et al. (2012). However, we found that the goodness of the fit was somewhat better when using the exponential curve in the vast majority of the analyzed data, so we chose to use the exponential curve as a best fit for the stray light correction. We then subtract this best fit stray light spectrum from each pixel in the slit (along the sample axis). All negative values in the scattered sunlight corrected spectra are treated as zeros. An example of the effect of this procedure for a given spectrum at one pixel (sample 100, line 50) of one particular pure night side image cube (VIR0383_00) is shown in Fig. 1.

Also shown in Fig. 1 is an example stray light spectrum obtained by averaging all valid data (*i.e.,* pixels not exhibiting error flags) obtained from observations at least 200 km above the limb of the planet for this same pure night side image cube. We see that the stray light present at 1.74 µm and 2.30 µm is nearly negligible. So, even if our simple exponential stray light correction is invalid, it will introduce negligible error in the current analysis. Future analysis of the near surface windows will require us to apply a more rigorous stray light correction, perhaps similar to that described by Kappel et al. (2012). Though the stray light has minimal effect at the wavelengths investigated in this paper, we include this description of our stray light correction process in order to document this method and to allow reference to it from future work that we intend to carry out.

Following the correction for the scattered light, in order to normalize the observations for long-term cross-comparisons, we apply a limb darkening correction to the data. In previous work, McGouldrick et al. (2008, 2012) utilized the corrections of Carlson et al. (1993). Here, we capitalize upon the efforts by Longobardo et al. (2012) to quantify the limb darkening seen in the VIRTIS-M-IR data in several of the near infrared spectral windows. Longobardo et al. (2012) found variations in the limb darkening be-

---

[1] A muntin is a bar or rigid supporting strip between adjacent panes of a glass window; formerly used to increase the structural integrity of a large window, today mostly used for decorative purposes.
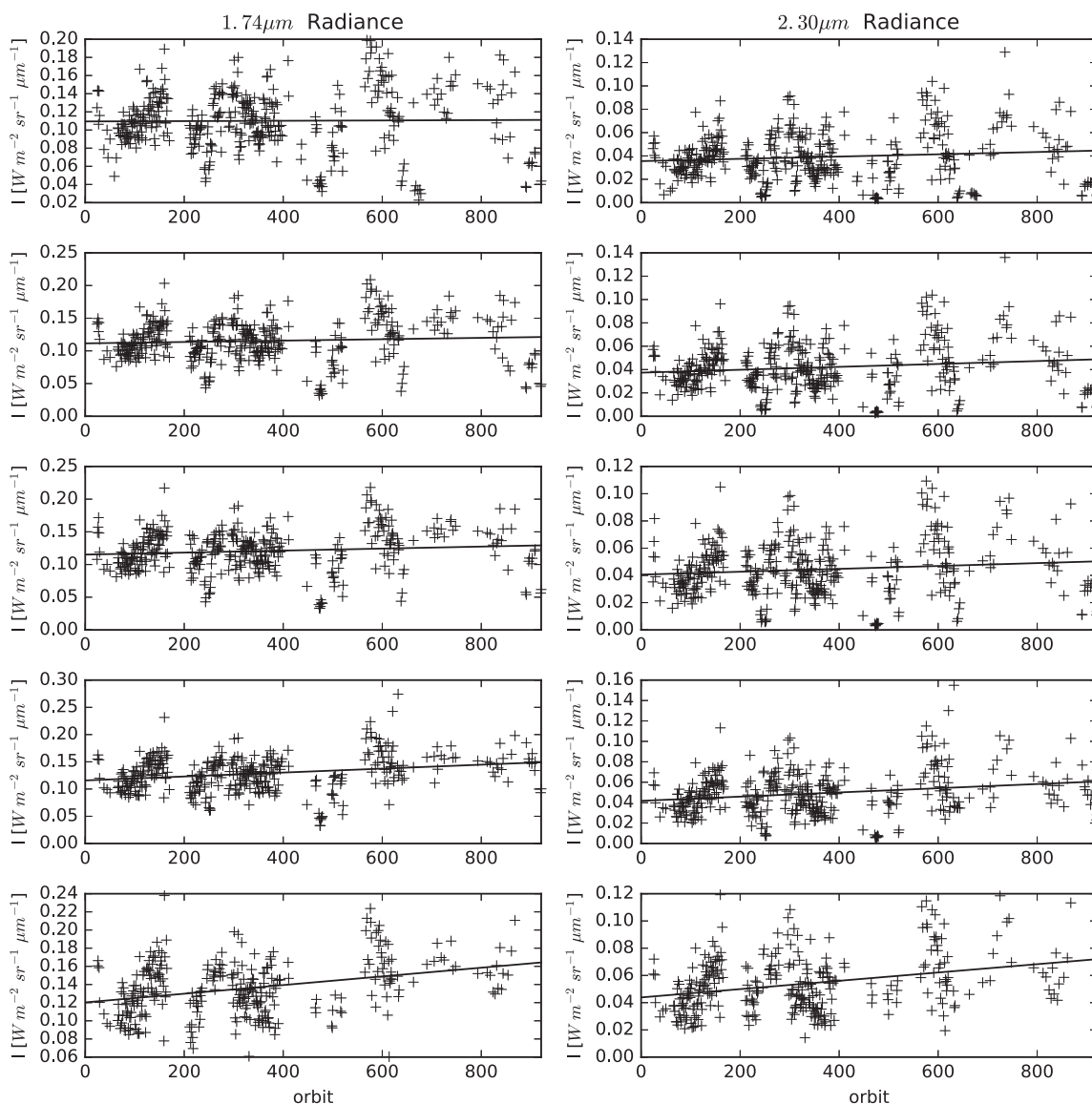
**Fig. 2.** Southern hemisphere radiance averaged across all cubes per orbit during the lifetime of VIRTIS-M-IR for both the 1.74 μm and 2.30 μm windows. From top to bottom, the rows represent data subject to differing minimum solar incidence angle restrictions of 95°, 100°, 105°, 110°, and 115°, respectively (0° is Sun at zenith).

havior as a function of latitude. For the windows that Longobardo et al. (2012) analyzed and that we study here, we use the "average" limb darkening correction parameters to determine a nominal radiance at zero emission angle:

$$I_{emitted} = I_{observed} \cdot (\alpha_\lambda + \beta_\lambda \cos\theta_e)^{-1}. \qquad (4)$$

## 3. Results

### 3.1. Long-term global tendencies

Bullock and Grinspoon (2001) and others have suggested that changes in $SO_2$ in the upper atmosphere could lead to changes in overall cloud coverage, due to a greater availability of condensable materials. Orders of magnitude variations are seen in the $SO_2$ concentrations above 70 km (Esposito et al., 1988; Marcq et al., 2012). Although the concentrations at those altitudes are only at the tens to hundreds of ppbv (parts per billion by volume) level, the scale height of the $SO_2$ at those altitudes has been measured to be about 1 km, indicating that an orders of magnitude larger concentration at the tens to hundreds of ppmv (parts per million by volume)

level exists deeper in the atmosphere in the cloud formation regions (near 62 km at equatorial latitudes). Thus, large changes in $SO_2$ could to have significant effects on the total mass loading of the photochemical clouds, and potentially also effects on the total mass available to form the deeper condensational cloud.

Our first goal is to determine whether a long-term global trend of Venusian cloud cover is evident in the VIRTIS-M-IR data set by examining the long-term trends of the radiance in the 1.74 μm and 2.30 μm atmospheric windows. In Fig. 2, we show the hemispherically averaged radiance for each of these two windows as a function of orbit number. Also shown in the figure is a linear best fit to the data, with free parameters $I_0$ (the radiance at orbit zero), and $m_I$ (the slope of the radiance per orbit). Finally, the five rows represent the five incidence angle cutoffs we considered in this analysis (95°, 100°, 105°, 110°, and 115°).

The linear fits to the data produce radiance at orbit 0, and the average slope of the radiance in units of W m$^{-2}$ sr$^{-1}$ μm$^{-1}$ per orbit (or per day), as well as one sigma standard deviation uncertainties in those parameters. We overplot the best fit trend line (but not the uncertainty information) in Fig. 2. The unaveraged data for both windows and at most incidence angle restrictions
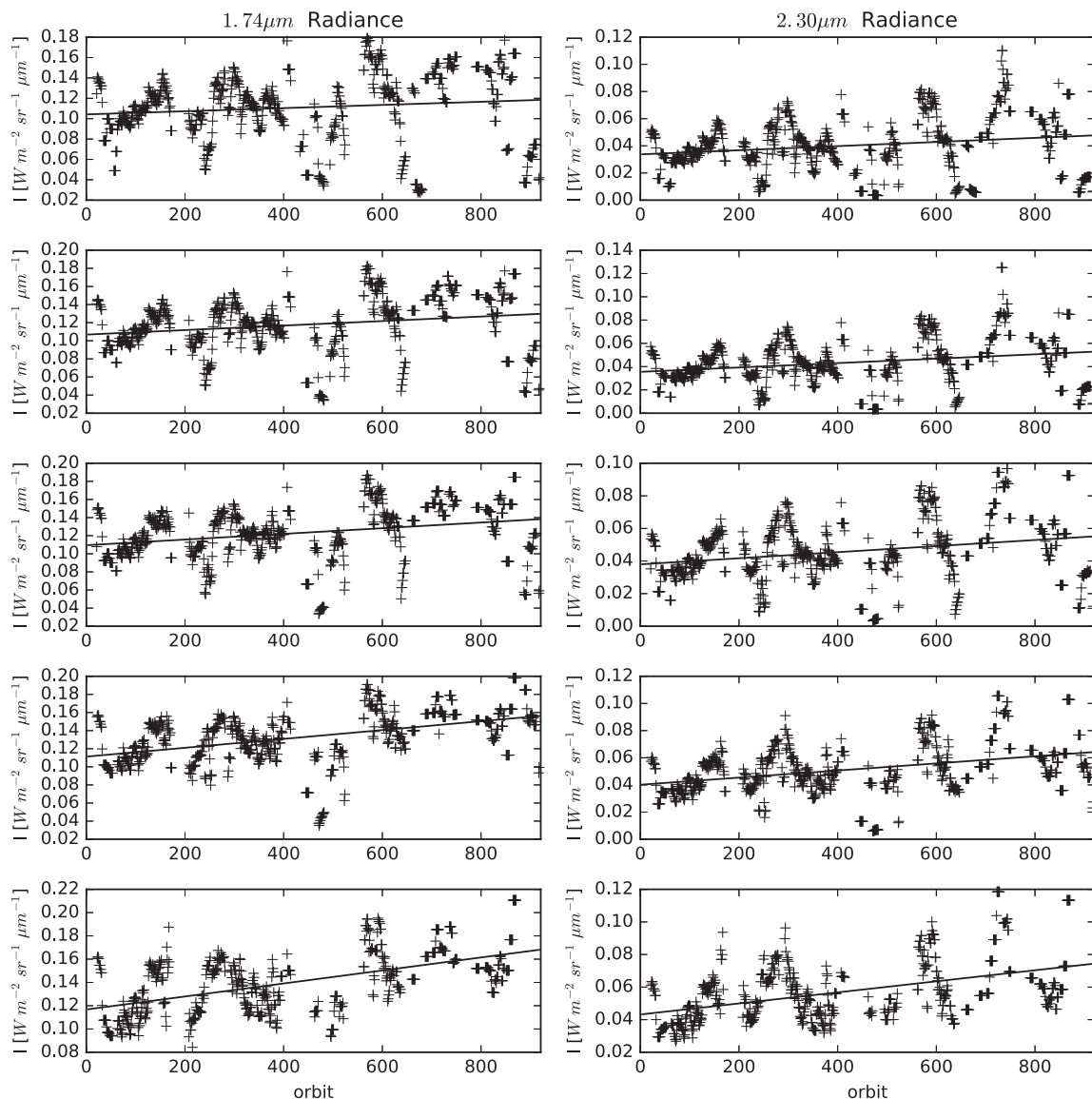
**Fig. 3.** Southern hemisphere radiance averaged across all cubes per orbit during the lifetime of VIRTIS-M-IR for both the 1.74 µm and 2.30 µm windows, but further averaged with a seven day moving window to approximate a global average radiance. As in Fig. 2, from top to bottom, solar incidence angle restrictions of 95°, 100°, 105°, 110°, and 115°, are represented.

shown in Fig. 2 shows a significant amount of scatter, and a best fit linear trend line that is essentially flat, indicating that there is no significant global change to the observed condensational cloud cover on Venus over the 2.5 year lifetime of the VIRTIS-M-IR instrument. Note also that as the incidence angle cutoff is made more restrictive, a hint of a periodicity begins to emerge from the data. However, since the larger emission angles selectively remove observational data from the polar regions, it is unclear at this point whether the periodicity exists throughout the southern hemisphere but has been masked by noise near the terminator, or whether is a more regional phenomenon.

Because of the high level of scatter in the data, which is partly due to the small field of view of the instrument making it difficult to observe the same region of the atmosphere from orbit to orbit, as well as the intrinsic variability within the clouds, in Fig. 3 we have smoothed the data with a seven-day box car mean window. A seven-day averaging of the data approximates extending the averaging over orbit done in Fig. 2 to a global average, since the period of rotation at the altitudes of these clouds is approximately seven days (Hueso et al., 2015).

However, upon applying a seven day moving window average of the data, we notice in Fig. 3 the appearance of slight trends to the mean radiance in each window, and evidence of shorter-term (on the order of weeks to months) variations in the cloud cover from radiance changes. The overall increase in radiance indicated by the mission-long linear best fit trend lines suggest that the overall cloud cover of Venus may have been thinning during the course of the mission. However, visual inspection of the plots indicates that for most incidence angle cutoffs this apparent trend is small compared to the overall scatter in radiance that is observed on an observation-to-observation basis. If the decrease in the $SO_2$ observed is driven by a conversion into $H_2SO_4$ and thence into clouds, then the results presented here, though only of a 2.5 year duration, are inconsistent with that explanation, at least on the global scale. However, the highly spatially variable nature of the observed $SO_2$ variations, and of the thickness of the condensational clouds, means that a regional scale relationship cannot yet be ruled out.

The spectral registration of the VIRTIS-M-IR spectrometer varies with temperature (Moinelo et al., 2010), so that the mapping from
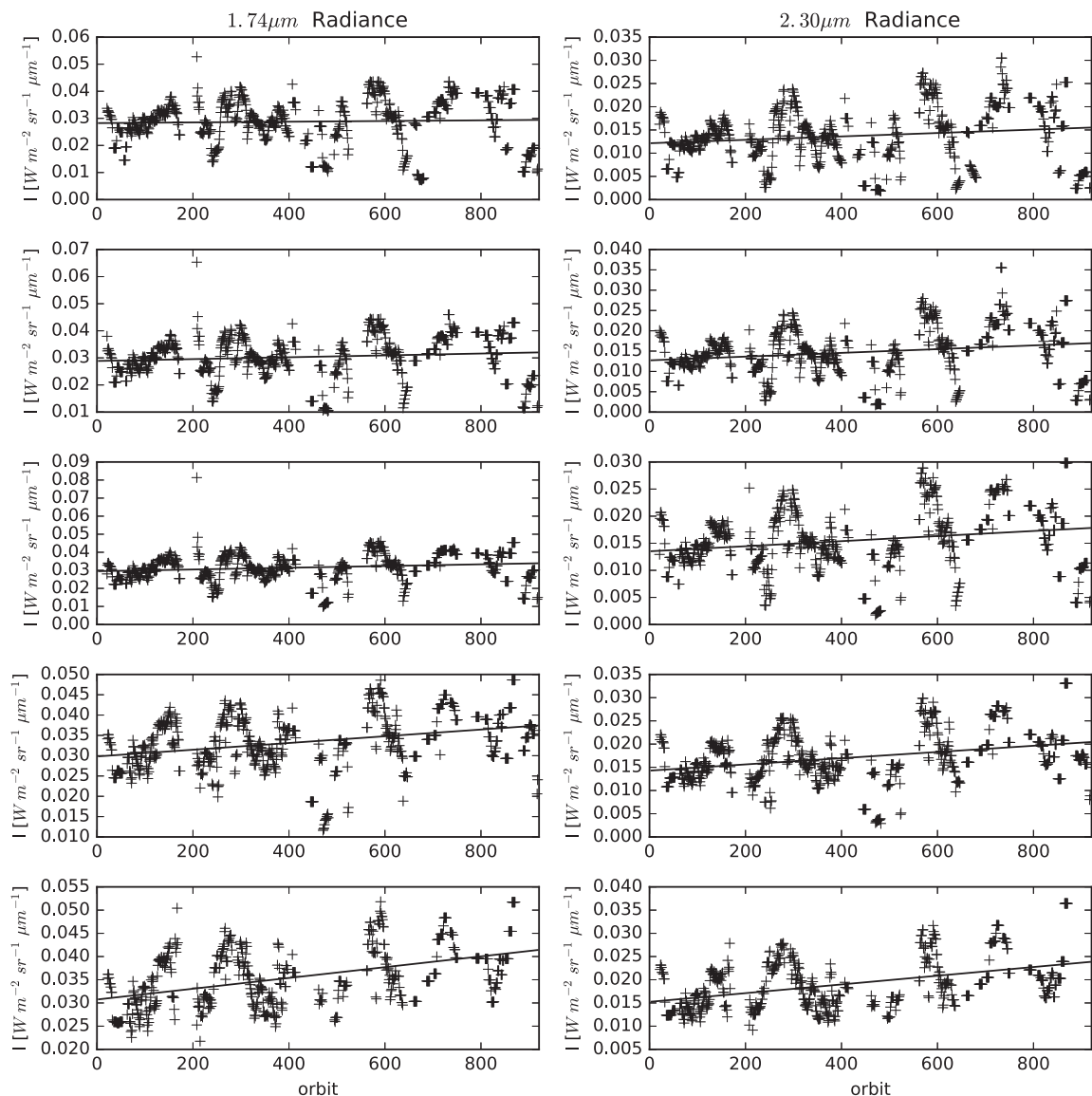
**Fig. 4.** Southern hemisphere radiance averaged across all cubes per orbit during the lifetime of VIRTIS-M-IR for both the 1.74 µm and 2.30 µm windows spectrally integrated across the entire spectral windows. The same incidence angle restrictions noted in Figs. 2 and 3 are represented.

band number to wavelength can vary with time. Thus, in generating the plots shown above, we use the radiance within the wavelength band that is closest to the defining wavelength for each particular data cube. These changes in band number associated with a particular wavelength can produce small but detectable variations in the measured flux. These variations are discussed at length by Kappel et al. (2012), who concluded that they are the result of errors in the ground calibration. Rather than reinvent the recalibration performed by Kappel et al. (2012), we attempt to rule out this so called Odd-Even effect as a source of the variations we see by additionally performing our analysis using data that have been spectrally integrated across the entire range of each spectral window. This is similar to what is described by McGouldrick et al. (2012), for the 1.74 µm window analyzed there. Here, we integrate the 1.74 µm window from 1.67 µm to 1.80 µm; and the 2.30 µm window from 2.15 µm to 2.60 µm. In this analysis of spectrally integrated data, the Even-Odd effect should be reduced, as overestimations of measured flux in half the bands will be roughly balanced by underestimations of the flux in the other half of the bands.

Fig. 4 shows the long term trends for the seven day averaging and spectrally integrated windows. We see that both the long-term trend of increasing radiance, as well as the periodic shorter-term variations appear in the integrated data. In fact, the relative magnitude of the day-to-day variations compared with the average radiance measured is slightly smaller for the integrated case, suggesting that the contribution to the measured radiance from the Odd-Even effect has been minimized by this integration, and that that effect is small for the present analysis. The data in Fig. 4 are best compared with the data in Fig. 3, since each has had the averaging extended across multiple orbits. Not shown, these similarities between the single band and integrated radiance for the unaveraged data are mirrored in the moving window averaged data.

### 3.2. Mission-long latitudinal mean radiances

One of our long-term goals in this project is to characterize the short-term behavior and variability of the condensational clouds of Venus. Previous work by McGouldrick et al. (2012) suggested that typical timescales of evolution were around 30 h, but
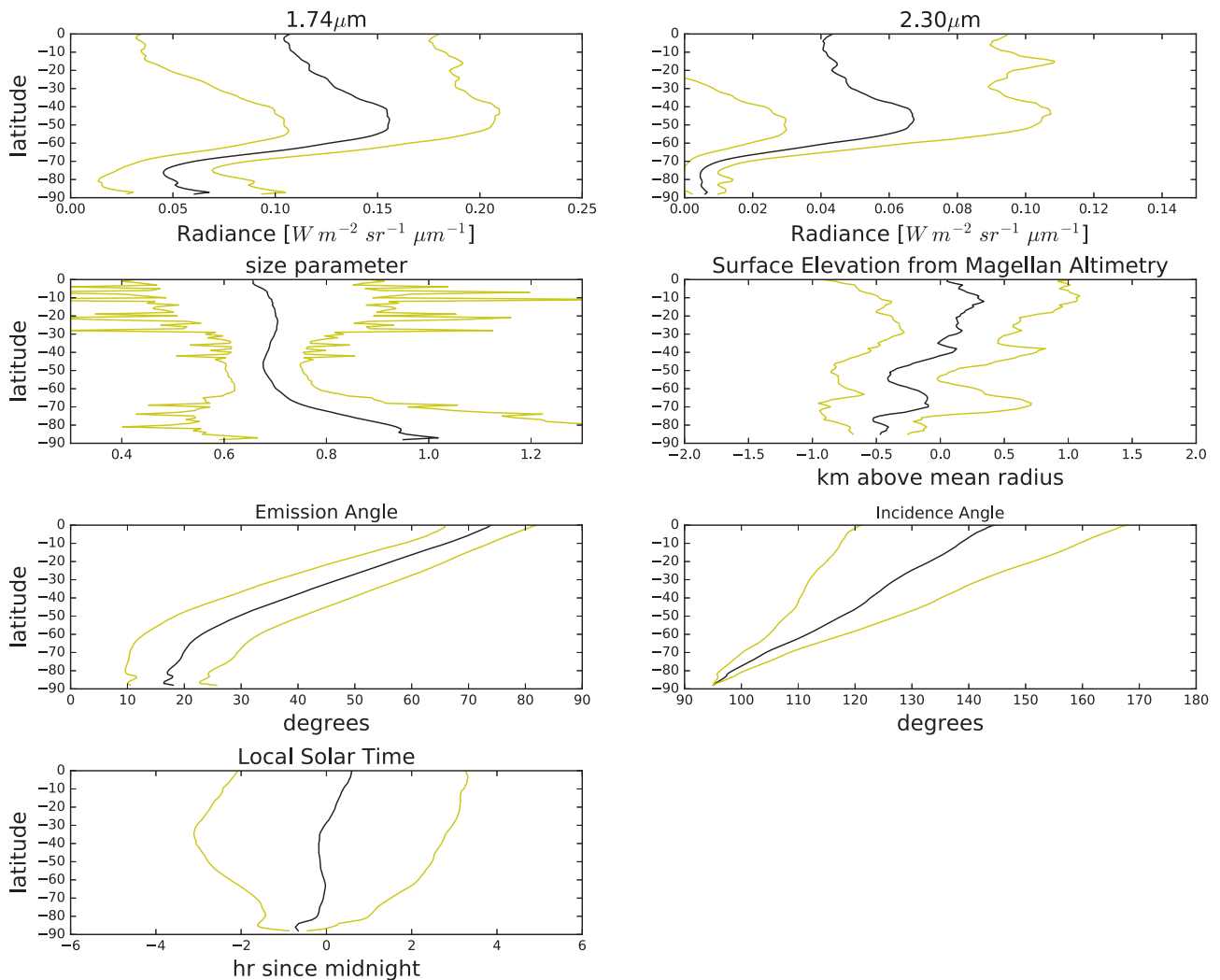
**Fig. 5.** Zonally and temporally averaged mean radiance with their standard deviations as functions of latitude for the 1.74 µm window, the 2.30 µm window, and the Carlson et al. (1993) size parameter, in addition to geometrical data such as incidence and emission angles, surface elevation, and local solar time. The data here are subject to a minimum incidence angle of 95°.

that work only analyzed two orbits' worth of observations. Part of the difficulty in establishing patterns of variability among the condensational clouds is in quantifying what level of variability can be attributed to cloud variations. For example, Carlson et al. (1993) showed that variations in the clouds produce roughly 20: 1 brightness contrast ratios at 2.30 µm and roughly 5: 1 brightness ratios at 1.74 µm. However, those contrast ratios do not account for the large magnitude of latitudinal variance in the clouds as indicated by radiance variations observed by Crisp et al. (1989) and Chanover et al. (1998). Within a given latitude region, the contrasts are about half of these global values. In previous analysis of short-term evolution of the clouds, McGouldrick et al. (2012) defined a cloud or hole boundary according to closed radiance contours at a 0.02 W m$^{-2}$ sr$^{-1}$ µm$^{-1}$ resolution. In order to reduce the arbitrariness of our cloud definition, we here develop a latitudinal profile of radiance for each of the windows, along with their one-sigma standard deviations. In future analysis of short-term cloud evolution, we plan to use these latitudinally resolved estimates of long-term variability to define the presence or absence of a local cloud or hole phenomenon.

In Fig. 5, we show the latitudinal profiles for each of the spectral windows. These figures assimilate the entire VIRTIS-M-IR dataset that fit our criteria detailed in Section 2 above. Note the local maximum in radiance evident near 50° latitude in both the

2.30 µm and 1.74 µm data. This has been seen since the NIR observations began in the 1980's, and has been explained as evidence of the interaction between the photochemical cloud production, the condensational cloud production, and the near-global meridional Hadley-like circulation by Imamura and Hashimoto (1998). The optically thick cloud near the polar collar is also evident as the strong decrease in radiance poleward of that radiance maximum. The slight but sharp increase in radiance very near to the pole in the 1.74 µm profile is possibly due to sunlight in the atmosphere scattered across the polar terminator, or is due to the deep emission from the polar vortex. In the 1.74 µm and 2.30 µm profiles, we also see a significant but smaller increase in the variability of the clouds (evidenced by an increase in the standard deviation about the mean) in the equatorial region. However, since the orbit of *Venus Express* limited the number of observations in this region that could match our criteria, and since these observations tend also to be very close to the limb – hence more susceptible to potential errors or uncertainties in the limb darkening correction – the variation seen at equatorial latitudes should be taken *cum grano salis*. It is hoped that observations by JAXA's *Akatsuki* spacecraft (Nakamura et al., 2007), having begun science operations from a more equatorial orbit in April of 2016, will help to resolve the level of variability seen here by VIRTIS-M-IR on *Venus Express* in the equatorial clouds of Venus.
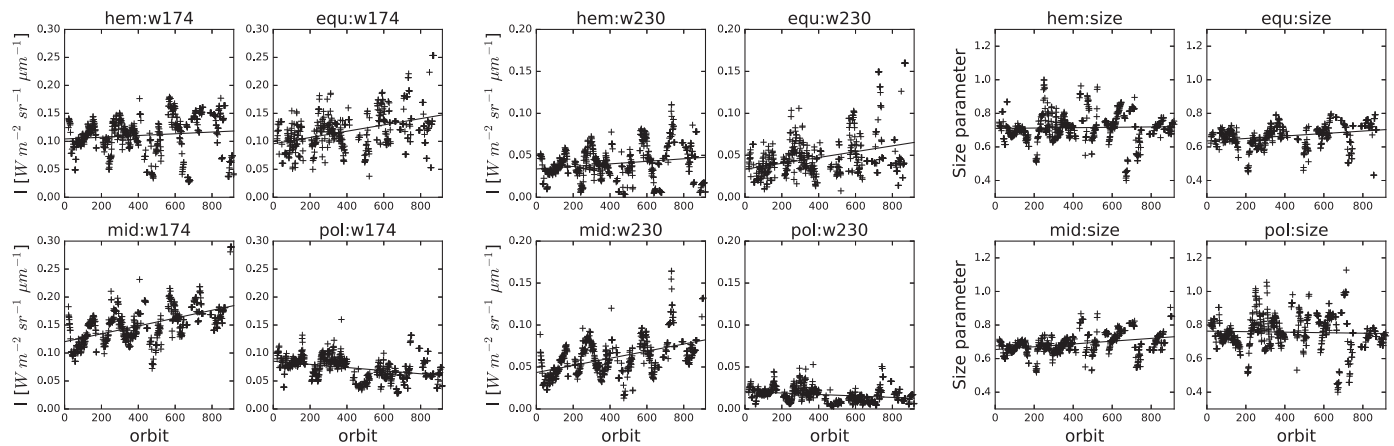
**Fig. 6.** Regionally segregated time series data for (L - R) 1.74 μm radiance, 2.30 μm radiance, and Carlson et al. (1993) size parameter, with seven-day averaging applied. The regions are: hemispheric ('hem': 0° − 90°), equatorial ('equ': 0° − 30°), mid-latitude ('mid':30° − 60°), and polar ('pol': 60° − 90°). Also shown is the best fit trend line to the observed data.

Also shown in Fig. 5 is the Carlson et al. (1993) size parameter:

$$m = \frac{I_{1.74\mu m}}{(I_{2.30\mu m})^{0.53}}. \tag{5}$$

Carlson et al. (1993) showed that this weighted ratio of the 1.74 μm and 2.30 μm emitted radiance can be used to estimate typical particle sizes in the Venus atmosphere, due to the relative Mie scattering properties of Mode 2 and Mode 3 particles at these wavelengths. Wilson et al. (2008) applied this technique to a handful of early orbits of *Venus Express*, and found a significant increase in size parameter in the polar regions, when applying a zonal average, similar to what we have done here, but for individual orbits. Similarly, Barstow et al. (2012) found that the ratio of the Mode 3:Mode 2′ particle numbers increased toward the pole. This increase is likely the result of the deeper altitude in which the condensational clouds exist at polar latitudes. We reproduce this strong increase in size parameter (hence, particle size) poleward of about 50°. We also see a slight increase in size parameter seen with a local maximum near 20° was not reported by Barstow et al. (2012). However, a reanalysis of the Barstow et al. (2012) work, presented in the Barstow (2012) doctoral thesis, does report a similar phenomenon with regard to the relative Mode 2′:Mode 3 particle number ratio. As can be seen in Fig. 5, the standard deviation about the mean is increasing at these latitudes, due to the paucity of data and large emission angle of the observations. Because we calculate the size parameter for a single band (we do not use the spectrally integrated calculations), the size parameter calculation is probably also still somewhat affected by the Odd-Even effect. If real, this increase could represent a slight increase in the relative population of Mode 3:Mode 2′ particles at these latitudes, followed by a reversal of the trend (*i.e.*, to an increase in Mode 2′ relative to Mode 3) from about 20° to about 50° latitude. Such a trend would be consistent with cloud formation altered by the meridional circulation modeled by Imamura and Hashimoto (1998). That is, the Mode 3 population would be driven by convection in the condensational clouds maximized near the equator, while the Mode 2 population would steadily increase as the parcels are carried from the equator toward the poles. Since the gravitational sedimentation velocity of the Mode 2 particles is so slow, they simply accumulate in the observable cloud, slowly skewing the population from larger to smaller particles, until the downwelling branch takes over near 50° latitude. However, this slight increase in the size parameter should also be taken with a grain of salt, since the large emission angle, low observation frequency, and possible calibration artifacts may still be playing significant roles in this calcu-

lation. Furthermore, the retrievals by Haus et al. (2014) did not find an increase in particles size at equatorial latitudes. It is anticipated that JAXA's *Akatsuki* spacecraft, observing from a more equatorial vantage point, will soon be able to resolve the veracity of this observation.

The average surface elevation observed in the data that satisfy our criteria shows that lower elevations are slightly favored in the polar regions compared with the elevations observed near the equatorial regions. However, the total range of average surface elevations observed is less than one kilometer. The emission and incidence angle profiles are as expected from a spacecraft imaging mostly the night side of a planet from a highly eccentric and polar orbit. Namely, low emission angle near the pole, while the equator is imaged mostly near the limb; and near-terminator (low incidence angles) near the poles, with gradually larger incidence angles at lower latitudes. The effect of the incidence angle on the measured parameters is negligible. The primary effect being a reduction in how far into the polar regions the analysis can obtain data that fit the incidence angle criterion. Therefore, we do not reproduce the latitudinal profiles for all incidence angle cutoffs.

### 3.3. Regional temporal behavior

Note again from Fig. 5 the significant changes in radiance as a function of latitude within all of the near infrared spectral windows. This large amount of variability, and the differing frequency of observation as a function of latitude suggests that we ought to consider geographic sub-regions when investigating possible existence of long term trends. Hence, we produce also zonally averaged radiance that have been averaged across 30° wide latitude bands, in addition to the hemisphere-wide calculations we showed in Section 3.1. We chose 30° wide regions for simplicity, and to ensure that we do not subsample the data to a point where the signal begins to be lost in the noise. We divide the southern hemisphere observations into polar (60°– 90°), mid-latitude (30°– 60°) and equatorial (0°– 30°) regions. Plots of these regionally averaged data are shown in Fig. 6 for the 1.74 μm and 2.30 μm radiance, and the Carlson et al. (1993) size parameter. The best fit linear trend parameters ($I_0$, $m_I$) and their uncertainties ($\delta I_0$, $\delta m_I$) for each of these regions and spectral windows are shown in Table 1. In addition to this, we calculate the total change in radiance expected from the beginning to the end of the 921-orbit VIRTIS lifetime, if the best fit trends were to persist throughout, and the total mission-long variability (standard deviation) of the radiance in each window and region.

**Table 1**
Parameters and their uncertainties to linear best fit to shown wavelength and region. Also included is the overall standard deviation. 'hem' represents the hemispheric average ($0° − 90°$); 'pol', 'mid', 'equ' represent $60° − 90°$, $30° − 60°$, and $0° − 30°$, respectively).

| region | $I_0$ | $\delta I_0$ | $m_I$ | $\delta m_I$ | $N_{orb} \times m_I$ | $\sigma_I$ | $p$-value |
|---|---|---|---|---|---|---|---|
| 1.74µm | W m$^{-2}$ sr$^{-1}$ µ$m^{-1}$ | | W m$^{-2}$ sr$^{-1}$ µ$m^{-1}$d$^{-1}$ | | W m$^{-2}$ sr$^{-1}$ µ$m^{-1}$ | | |
| hem | 1.094$e$ − 01 | 1.886e−03 | 1.821e−06 | 4.569e−06 | 1.677e−03 | 6.182e−02 | 0.0017 |
| pol | 9.083e−02 | 6.720e−04 | −3.584e−06 | 2.160e−06 | −3.301e−02 | 4.052e−02 | < 0.0001 |
| mid | 1.240e−01 | 3.896e−04 | 5.744e−05 | 8.338e−07 | 5.290e−02 | 5.212e−02 | < 0.0001 |
| equ | 9.923e−02 | 7.656e−04 | 5.622e−05 | 3.114e−06 | 5.178e−02 | 6.793e−02 | < 0.0001 |
| 2.30 µ$m$ | W m$^{-2}$ sr$^{-1}$ µ$m^{-1}$ | | W m$^{-2}$ sr$^{-1}$ µ$m^{-1}$d$^{-1}$ | | W m$^{-2}$ sr$^{-1}$ µ$m^{-1}$ | | |
| hem | 3.555e−02 | 5.508e−04 | 9.752e−06 | 1.157e−06 | 8.982e−03 | 4.055e−02 | < 0.0001 |
| pol | 2.331e−02 | 2.925e−05 | −1.256e−06 | 7.176e−07 | −1.157e−02 | 1.720e−02 | < 0.0001 |
| mid | 4.497e−02 | 3.554e−05 | 3.652e−05 | 7.472e−08 | 3.363e−02 | 3.741e−02 | < 0.0001 |
| equ | 3.456e−02 | 1.203e−04 | 3.619e−05 | 8.334e−07 | 3.333e−02 | 5.063e−02 | < 0.0001 |
| Size | < unitless > | | < unitless > d$^{-1}$ | | < unitless > | | |
| hem | 7.115e−01 | 3.750e−03 | 1.270e−05 | 9.594e−06 | 1.170e−02 | 2.053e−01 | 0.3720 |
| pol | 7.479e−01 | 2.588e−03 | 1.662e−05 | 7.172e−06 | 1.530e−02 | 2.687e−01 | 0.3087 |
| mid | 6.588e−01 | 1.266e−03 | 7.154e−06 | 3.374e−06 | 6.589e−02 | 8.933e−02 | < 0.0001 |
| equ | 6.448e−01 | 1.946e−03 | 5.195e−05 | 4.824e−06 | 4.784e−02 | 2.761e−01 | < 0.0001 |
| Elev | km | | km d$^{-1}$ | | km | | |
| hem | −1.799e−01 | 2.484e−02 | 9.167e−05 | 5.749e−05 | 8.443e−02 | 6.038e−01 | 0.0827 |
| pol | −2.170e−01 | 1.840e−02 | 2.911e−05 | 4.502e−05 | 2.681e−02 | 6.287e−01 | 0.2742 |
| mid | −2.342e−01 | 7.573e−03 | 1.260e−04 | 1.144e−05 | 1.160e−01 | 5.580e−01 | 0.2853 |
| equ | 2.358e−01 | 1.702e−02 | −4.717e−06 | 4.029e−05 | −4.345e−03 | 5.888e−01 | 0.5364 |
| Emis | < deg > | | < deg > d$^{-1}$ | | < deg > | | |
| hem | 3.045e+01 | 7.891e−02 | 4.124e−03 | 2.425e−04 | 3.798e+00 | 1.692e+01 | 0.0585 |
| pol | 2.017e+01 | 1.628e−01 | 9.252e−04 | 5.886e−04 | 8.521e−01 | 9.383e+00 | 0.0139 |
| mid | 3.225e+01 | 5.829e−02 | 6.935e−03 | 1.004e−04 | 6.387e+00 | 1.289e+01 | 0.0394 |
| equ | 5.436e+01 | 7.993e−02 | 1.103e−02 | 1.597e−04 | 1.016e+01 | 1.181e+01 | 0.0024 |
| Inc | < deg > | | < deg > d$^{-1}$ | | < deg > | | |
| hem | 1.147e+02 | 1.132e−02 | −4.852e−03 | 1.465e−04 | −4.469e+00 | 1.537e+01 | 0.1937 |
| pol | 1.059e+02 | 5.452e−02 | −3.563e−03 | 1.294e−04 | −3.281e+00 | 5.886e+00 | < 0.0001 |
| mid | 1.173e+02 | 1.240e−02 | −4.885e−03 | 6.183e−05 | −4.499e+00 | 1.174e+01 | 0.0262 |
| equ | 1.272e+02 | 8.688e−02 | −2.186e−03 | 1.595e−04 | −2.013e+00 | 1.862e+01 | 0.0843 |
| LST | h | | h d$^{-1}$ | | h | | |
| hem | −8.239e−01 | 8.726e−05 | 1.467e−03 | 1.703e−07 | 1.351e+00 | 2.458e+00 | 0.0017 |
| pol | −5.108e−01 | 9.058e−05 | 5.384e−04 | 1.833e−07 | 4.959e−01 | 1.661e+00 | 0.2154 |
| mid | −7.590e−01 | 4.815e−05 | 1.492e−03 | 1.020e−07 | 1.374e+00 | 2.682e+00 | 0.0056 |
| equ | −1.506e+00 | 1.205e−04 | 3.028e−03 | 5.436e−07 | 2.789e+00 | 2.920e+00 | < 0.0001 |

Our strictest criterion for considering a best fit trend (slope) to be significant requires that the total change in radiance predicted from the slope of the fit (*i.e., $N_{orbit} \times m_I$*) exceeds the overall variability in (*i.e.,* the standard deviation of) the measured emitted radiance ($\sigma_I(\phi)$). That is, the trend is significant only if the long term trend exceeds the per-observation variations. Note that, as expected from the hemispherical averages, the majority of the windows and regions exhibit best fit trends that are consistent with a null result; that is, no change in overall cloud coverage. In fact, only the mid-latitude 1.74 µm radiance indicates a significant long-term trend by this criterion. However, the mid-latitude region at 1.74 µm and 2.30 µm, and the size parameter, all exhibit overall tendencies in that are suggestive of long-term trends in cloud thickness or particle size population. But, even these long-term variations require several years at their currently measured rates to effect a significant difference in the overall emitted radiance, hence cloud cover, based on this criterion. A longer time baseline as might be provided by the *Akatsuki* mission could elucidate the persistence or transience of these long-term trends and their significance.

Another method of testing the significance of the linear trend is to apply a linear regression analysis to evaluate the correlation between the estimated trend line and the data, compared with the null hypothesis. We calculate the *p*-value, which is a measure of the probability that random variations can explain the observed distribution as well as the modeled trend. Hence, a *p*-value of 0.01 indicated that there is a 1% likelihood that the observed data are better fit with random perturbations, and a 99% likelihood that the best fit trend is a better predictor of the observed behavior. While a small value of the *p*-value can be interpreted to mean the null hypothesis is highly unlikely, it cannot confirm the existence of the posited trend. However, a large *p*-value can be used to rule out a linear trend in the data. Here, we will assume that a *p*-value of less than 0.0001 (a 99.99% likelihood that the best fit trend line is a better predictor of the observed changes than random variations) indicates that the trend based on the best fit parameters is likely to be real. The rightmost column in Table 1 shows the calculated *p*-value for each of the parameters and regions analyzed in this paper. We find that the *p*-value for the 1.74 µm and 2.30 µm radiance data in all regions is less than 0.002, and is less than 0.0001 in all but the 1.74 µm hemispherical data. We find *p*-values for the size parameter to be less than 0.0001 in the mid-latitude and equatorial data; but larger than 0.3 for the hemispherical and polar data, suggesting that the trends a lower latitudes are more reliable than those at high latitude or planet-wide. However, the calculated trend in the hemispheric and polar size parameter data
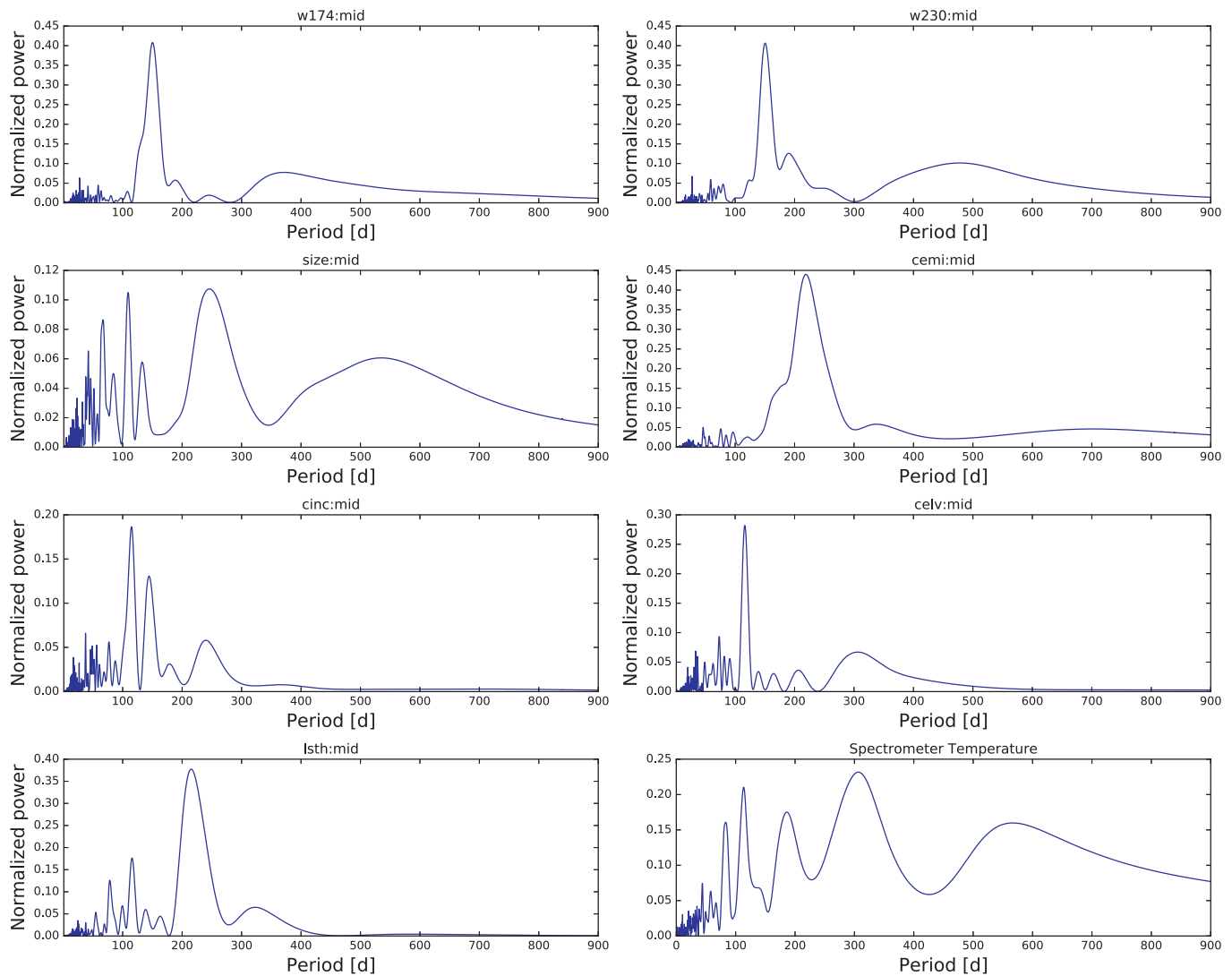
**Fig. 7.** Frequency spectrum for the mid-latitude 1.74 µm and 2.30 µm radiance, Carlson et al. (1993) size parameter, emission and incidence angles, surface elevation, local solar time, and spectrometer temperature.

is very shallow, so there is very little difference between the linear best fit and the null hypothesis, once the overall average has been corrected for. Finally, among the geometric parameters analyzed (emission angle, incidence angle, surface elevation, and local solar time), all but a few of the quantities demonstrate relatively large $p$-values, indicating at least that the linear best fit trends to these quantities are less statistically significant than those discussed above. Furthermore, the absence of significant linear trends found in these parameters suggests that it is unlikely that variations in these geometric parameters are responsible for the long-term trends observed in the radiance data.

### 3.4. 150 day oscillation in the mid-latitudes

In addition to these long-term trends, a months-long periodic variation can be seen in the mid-latitude region for the 1.74 µm and 2.30 µm data. Such a periodicity is most noticeable for larger incidence angle restrictions and at mid-latitudes, and was previously suggested by McGouldrick et al. (2012) using a somewhat smaller subset of this data; it is reinforced here with the full dataset. This periodicity is not seen at the shorter wavelengths that are less cloud dominated and more surface dominated. However, this may be a function of our stray light removal technique. Fur-

ther analysis of the variability of these surface dominated windows is underway. McGouldrick et al. (2012) qualitatively estimated a period of about 140 days. Here, in order to quantitatively determine the periodicity, we applied a least squares sinusoidal fit analysis (LSSA) (Lomb, 1976; Scargle, 1982) to produce a frequency spectrum of the 1.74 µm radiance, shown in Fig. 7. We perform the LSSA calculation by starting with the time series data shown in Fig. 3, and subtracting the linear trend for the 1.74 µm mid-latitude data shown in Table 1, in order to achieve a data set with a mean of zero. We then apply the LSSA calculation to this adjusted radiance data.

Fig. 7 shows the LSSA frequency analysis for the mid-latitude ($30° − 60°$) data at 1.74 µm, 2.30 µm, the Carlson et al. (1993) size parameter, and several geometric parameters, with the seven-day averaging applied (*i.e.,* the data shown in Fig. 3). As discussed previously, the seven-day moving average is designed to minimize the regionalism that results from the limited field of view of the VIRTIS-M instrument. By thus averaging the data, we arrive more closely at a measure of the zonally averaged behavior. However, as we will show later, this averaging to ensure a zonally averaged radiance does not appear to affect the values of the measured periods significantly. One period stands clear above all others in each of the 1.74 µm and the 2.30 µm radiance data pe-

**Table 2**
Summary of most prominant period found for each parameter for each tested incidence angle restriction, and each size of the moving window averaging. All units of periods are in days.

| window | $\min(\theta_{inc})$ | $I_1$ | $I_2$ | size | $\theta_{emi}$ | $\theta_{inc}$ | elevation | LST |
|--------|----------------------|-------|-------|------|----------------|----------------|-----------|-----|
|        | 95°  | 147.4 | 146.9 | 109.2 | 216.7 | 116.8 | 116.8 | 215.9 |
|        | 100° | 147.3 | 146.8 | 109.6 | 215.8 | 117.0 | 116.6 | 215.5 |
| 1      | 105° | 146.7 | 146.4 | 41.7  | 212.7 | 118.8 | 116.8 | 215.5 |
|        | 110° | 146.6 | 146.2 | 253.5 | 213.8 | 119.6 | 116.7 | 212.1 |
|        | 115° | 144.6 | 145.3 | 247.9 | 211.4 | 145.2 | 119.6 | 232.1 |
|        | 95°  | 150.3 | 150.5 | 245.9 | 219.0 | 114.9 | 116.3 | 215.2 |
|        | 100° | 149.9 | 150.3 | 108.9 | 218.5 | 115.7 | 116.0 | 215.1 |
| 7      | 105° | 149.7 | 150.0 | 108.8 | 218.0 | 147.4 | 116.0 | 214.7 |
|        | 110° | 149.7 | 149.9 | 109.0 | 217.6 | 148.7 | 116.0 | 214.4 |
|        | 115° | 146.6 | 148.8 | 258.4 | 217.4 | 76.8  | 117.2 | 227.1 |
|        | 95°  | 150.7 | 151.0 | 254.0 | 218.8 | 113.6 | 116.2 | 215.9 |
|        | 100° | 150.4 | 150.8 | 262.1 | 219.2 | 145.4 | 116.2 | 215.8 |
| 14     | 105° | 150.3 | 150.8 | 109.1 | 219.6 | 146.1 | 116.0 | 215.6 |
|        | 110° | 150.3 | 150.7 | 259.3 | 219.2 | 147.1 | 115.9 | 215.3 |
|        | 115° | 145.8 | 148.8 | 265.9 | 218.8 | 76.7  | 117.1 | 226.5 |

riodograms. At 1.74 µm, this period is found to be 150.3 days, while at 2.30 µm it is found to be 150.5 days. This peak is rather broad, with a half-width of about 20 days, indicating either that this is a quasi-period, whose frequency varies with time, or we have too short a baseline of data for a more precise measurement of the frequency spectrum. It is possible that wavelet analysis (Bravo et al., 2014) of this dataset may resolve this discrepancy; but it is subject to the same difficulties of the sporadic nature and somewhat brief temporal duration of the observations.

Also shown in Fig. 7 is the periodogram for the Carlson et al. (1993) size parameter. There are no dominant peaks with significant power in the frequency spectrum. Since our calculation of the size parameter involves a comparison of radiance at two separate bands, it is likely that the odd-even effect discussed by Kappel et al. (2012) may have more of an effect here. Not only might the radiance in one of the bands fall into an enhanced or a reduced sensitivity pixel of the detector, but since the wavelength registration is non-linear, it is possible that the odd versus even location of each band might not occur in parallel. That is, one band might be enhanced while the other is reduced. This is possibly also the reason for the larger and more variable standard deviation found in the latitudinal profile of the size parameter data compared with the radiances themselves, as seen in Fig. 5. The lack of a significant peak in the size parameter periodogram around 150 days indicates that changes in the relative populations of Mode 2′ and Mode 3 particles in the clouds of Venus are not likely to be driving the observed periodicity at 1.74 µm and 2.30 µm.

We compare also the periodograms of various geometrical parameters of the observations, including incidence angle, emission angle, surface elevation, and local solar time. None of these show a significant peak near 150 days, suggesting that changes in the viewing geometry are not responsible for the periodicity seen at 1.74 µm and 2.30 µm. Notably, the LSSA periodogram does find strong evidence for periodicity in several of the geometric parameters, For example, the emission angle and the local solar time show a strong period at about 220 days and 216 days, very close to the 225 day sidereal orbital period of Venus. This is not surprising, since these are both tied to the viewed phase of Venus by VIRTIS-M-IR, which evolves in parallel with the orbit of Venus around the Sun. In addition, the solar incidence angle and the surface elevation shows a significant peak at 115 days and 116 days, almost exactly the Venusian synodic (or solar) day of 116.75 days, as expected. Since the observations in the present analysis are restricted to the night side, and the view of the surface of Venus from VIRTIS will vary along with the orbit of Venus around the Sun, then the

surface data that fit our criteria should be seen on a periodicity very closely tied to the synodic period of Venus, or the solar day. That the LSSA finds these periodicities in the geometry data that match what would be expected *a priori*, from the known orbital and observational parameters and criteria, lends further credence to the veracity of the periods measured in the analysis of the radiance data and their absence in the size parameter data.

Finally, we also compare the periodogram of the spectrometer temperature to the observed radiance variations. Since the wavelength registration of the spectrometer is temperature dependent, and there is evidence for remaining imperfections in the calibration of the detector (Kappel et al., 2012; Moinelo et al., 2010), changes in the spectrometer temperature might produce spurious changes in measured radiance. However, Fig. 7 shows that the LSSA found no dominant period in the spectrometer temperature. Other relevant instrumental temperatures are measured and reported by the VIRTIS housekeeping, including the focal plane temperature, telescope temperature, and cooling point temperature. We do not reproduce those analyses here because each shows nearly identical periodogram spectra, even as the magnitudes of the temperatures are significantly different.

We have run the LSSA analysis for a number of different averaging window sizes, incidence angle cutoffs, and frequency space resolutions. Although the specific values of the periods change slightly in response to changes in the incidence angle criterion and the size of the averaging window, the salient points mentioned in the discussion of Fig. 7 remain unchanged through each of these. That is, an oscillation is found in the 1.74 µm and 2.30 µm radiance with a period of about 150 days. None of the other measured or calculated quantities exhibit a dominant periodicity with a similar frequency. The emission angle and local solar time show periodicities of approximately the Venus sidereal orbital period. And the surface elevation and solar incidence angles show periodicities of approximately the Venus synodic period, or solar day. The results of these calculations are summarized in Table 2.

In order to further quantify and characterize the observed variability, in Fig. 8, we produce period-folded plots of the parameters analyzed in Fig. 7. Here, we see that the amplitude of the periodic behavior is approximately as large as the magnitude of the per-observation variability seen in the data. By phase-shifting the period-folded 1.74 µm radiance by about 45 days, we can see that the variation can be well matched with a sinusoid with an amplitude that is half of the maximum radiance measured. The phase folded data suggest that the sinusoids describing the near infrared radiance variations may not be quite symmetric. That is, the comparison suggests that the decrease in radiance might occur slightly
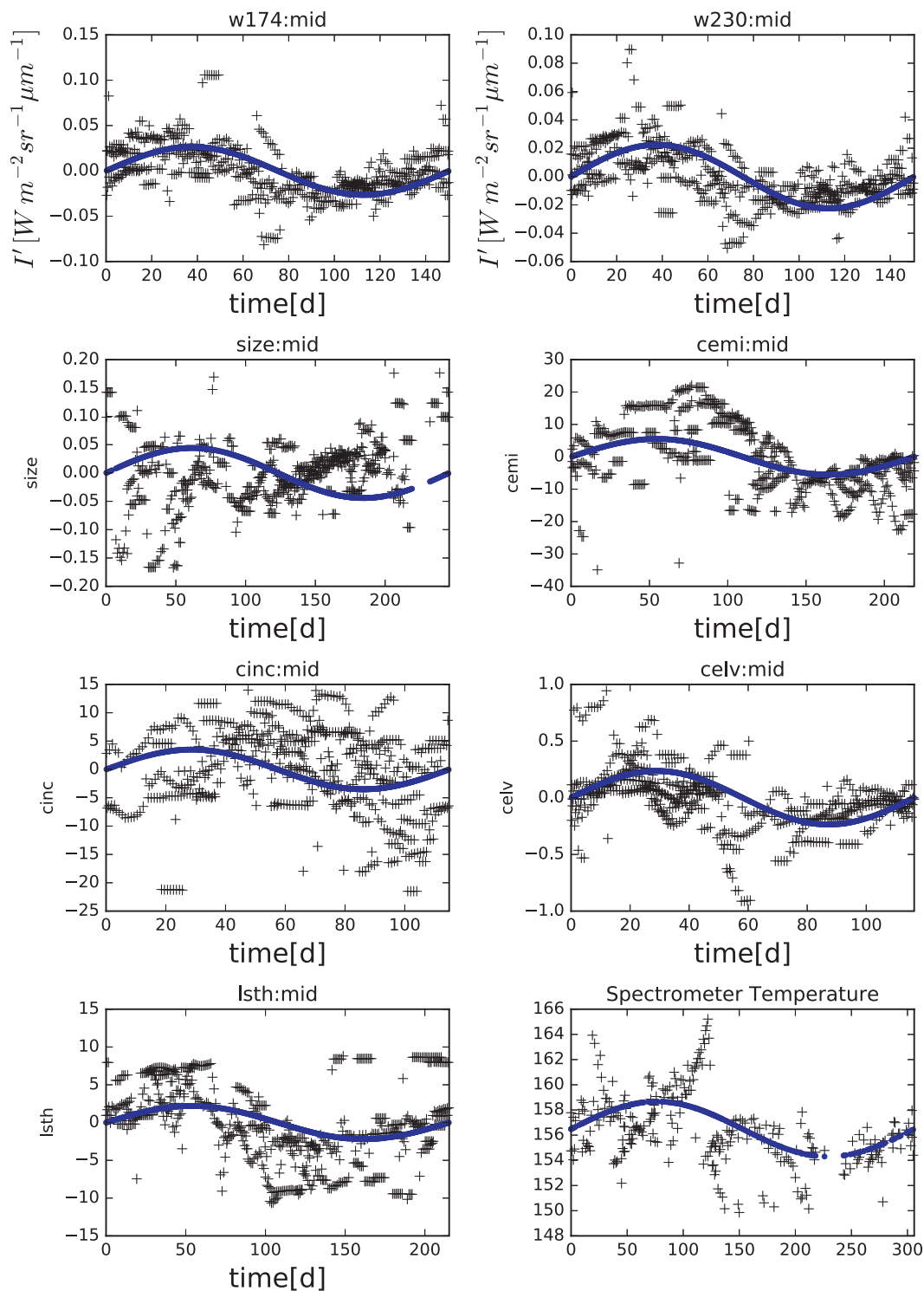
**Fig. 8.** Phase-folded data for the mid-latitude data, for each of the parameters shown in the previous figures, with seven-day averaging applied, assuming the period found by LSSA having the greatest spectral power for each parameter. The radiance curves are phase shifted by 45 days to align with the baseline sinusoid. Phase shifts of −75 days, 25 days, 30 days, −50 days, and 45 days have been added to the plots of size parameter, emission angle, incidence, angle, surface elevation, local solar time, and spectrometer temperature, respectively.

more quickly than the corresponding increase. In Section 4, we consider potential drivers of the observed variations, and a difference in the rate of increase or decrease in radiance can help to discriminate among the possibilities. However, since the difference between a standard and a skewed sinusoid is so slight, compared with the data, we do not make any conclusions based on the shape of the curve at this time.

## 4. Discussion

Here we explore some various drivers of the observed variations and consider their likelihood, based on the analyzed data set and other constraints.

We report a possible long-term increase in 1.74 µm and 2.30 µm radiance at mid-latitudes, that would indicate an over-

all reduction in total cloud opacity in this region. This increase in mid-latitude radiances is accompanied by a decrease in polar radiances. On a hemisphere-wide averaging, there is little change seen in these radiances over the course of the VIRTIS-M-IR instrumental lifetime. These trends are not consistent with a scenario in which the observed decrease in $SO_2$ at higher altitudes reported by Marcq et al. (2012) is coupled with a conversion of $SO_2$ into $H_2SO_4$ and thence into clouds. Hence some other sink for the $SO_2$ loss observed must be found. However, as the observed trends are barely larger than the overall variance in the data, more detailed analysis of this and future data (including the *Akatsuki* mission) will be required for more definitive conclusions.

Previous investigations have reported increases in wind speeds in the Venus atmosphere over time (Khatuntsev et al., 2013; Kouyama et al., 2013). These investigations interpret motions of high contrast features in the reflected sunlight at ultraviolet wavelengths as indicators of local wind speeds at an altitude of the cloud tops, around 70 km above the surface of the planet. There remains some ambiguity as to whether these measured winds are indicative of the true wind speeds of the features themselves, or of the large scale dynamics (similar to the "steering winds" at 500 mb on Earth that transport tropical and extratropical cyclones), or of morphological or compositional changes. However, if we accept that the measured wind speeds are representative of the overall dynamics of the Venus atmosphere, then the increase in the mean zonal wind speeds reported by both Khatuntsev et al. (2013) and Kouyama et al. (2013) would imply that some mechanism is acting that either adds momentum to the atmosphere as a whole, or transports momentum from another atmospheric region to the level of the cloud tops seen in ultraviolet wavelengths. If momentum is being transported to this region of the atmosphere, then so too must energy be transported. Such a transport of energy could manifest itself as an increase in local temperature at regions where the clouds have been accelerated by the deposition of momentum. Another possibility is that the energy could be transported in the form of latent heat, but the very small mass of the Venus clouds tends to preclude latent heat as an efficient means of energy transport. Because the vapor pressure of the sulfuric acid cloud particles is so small, small changes in temperature tend to have rapid and significant effects on the mass and opacity of the Venus clouds (McGouldrick and Toon, 2007). This increase in radiance emitted from the cloud-dominated spectral windows at equatorial and mid-latitudes, coupled with the decrease in radiance at polar latitudes could indicate a net transport of energy from high to low latitude over the course of these observations. Such an energy transport would be consistent with the increase in momentum seen by Khatuntsev et al. (2013) and Kouyama et al. (2013). It is beyond the scope of this paper to thoroughly compare the variation in the previously measured wind speeds at the cloud tops using VMC ultraviolet data with the emitted radiance through the condensational (and photochemical) clouds of Venus using VIRTIS infrared data, but we note that the appearance of a correlation suggests fertile ground for future comparison.

We might consider that this 150-day oscillation is a manifestation of a Hadley-like meridional circulation in the clouds. If we consider a meridional circulation cell that runs from the equator to about 50° latitude, consistent with previous models by Imamura and Hashimoto (1998), then we calculate an average meridional wind speed of only 0.9 m/s. Hueso et al. (2015; 2012), using VIRTIS-M-Vis ultraviolet observations, and Khatuntsev et al. (2013), using VMC ultraviolet observations, report meridional wind speeds peaking at about 10 m/s in the poleward direction at a latitude of around 50°–55°, and decreasing to 0 m/s at the pole and equator. They each interpret this as a manifestation of a hemispherical-scale Hadley-like meridional circulation cell. If we assume a sinusoidal shape to the meridional wind speed as a function of latitude,

then we can estimate the average flow speed over the entire cell to be about 6 m/s. Hence, the timescale for the Hadley-like meridional circulation would then be about 35 days, much shorter than the periodicity measured here. Note that Hueso et al. (2015) report measured meridional wind speeds of a few m/s in infrared wavelengths (corresponding to similar altitudes to those inhabited by the clouds that drive the radiance variations analyzed here). However, they also point out that their measured wind speed is significantly smaller than their measured standard deviations, indicating that the meridional circulation likely has its return branch at a deeper altitude than that occupied by the clouds. Hence, for the meridional circulation to directly affect the properties of the condensational clouds between about 50 km and 57 km that are analyzed here, there would need to be a vertical wander of the mean circulation. Similar wanderings of the meridional circulation were found in VenusCAM General Circulation Model simulations by Parish et al. (2011). However, subsequent analysis showed that a later version of VenusCAM that addressed a number of angular momentum errors did not show as significant a variation (Lebonnois et al., 2012).

The 150 day oscillation is closer in magnitude to the time scale for the meridional circulation assumed in the models of Imamura and Hashimoto (1998). Imamura and Hashimoto (1998) prescribed a meridional Hadley-like circulation with a cycle timescale of 90 days. This would correspond to a maximum mid-latitude meridional cloud top wind speed of a few m/s, or a factor of three or so smaller than the wind speed reported from the Venus Express observations described above. Based on the results of Imamura and Hashimoto (1998), who considered the effect of a variation in the magnitude of the meridional circulation, a meridional Hadley-like circulation with a 150 day timescale would produce smaller latitudinal contrasts in cloud opacity than those that are observed. This occurs because for slower circulations, particle sedimentation timescales become more important to the cloud particle lifetimes than the meridional transportation timescales. Note that the Imamura and Hashimoto (1998) models did not consider effects of the zonal circulation, having treated a 2D (latitude-altitude) model. The 2D cloud structure found by Imamura and Hashimoto (1998) was consistent with latitudinal opacity variations derived from the observations of Venus by Crisp et al. (1989) and Chanover et al. (1998), indicating that the magnitude of the meridional circulation that Imamura and Hashimoto (1998) proposed is consistent with observations. Our long-term average latitudinal profiles also are consistent with the previous work by Crisp et al. (1989) and Chanover et al. (1998), suggesting that the meridional circulation remains similar to that postulated by Imamura and Hashimoto (1998). However, our analysis does not investigate potential temporal variations in the latitudinal profile, which might indicate variations in the magnitude of the meridional circulation. It is difficult to achieve a high level of confidence in the temporal variations in latitudinal profiles using VIRTIS-M-IR data, because the spatial coverage is so limited. Perhaps the Akatsuki mission (Nakamura et al., 2016), with its more equatorially-inclined orbit, and frequent high spatial resolution full-disk imaging capability, might address this issue.

In addition to the long-term trend in the measured wind speeds, previous investigators such as Khatuntsev et al. (2013) and Kouyama et al. (2013) have indicated periodic variations in the wind speeds. Kouyama et al. (2013) reported a 255 day period in their measured wind speeds; but this does not seem to be related to the 150 day period found here. Furthermore, their analysis does not find a comparable periodicity near 150 days. Khatuntsev et al. (2013) reports on a number of short-period ($4 - 5$ days) oscillations in their measured wind speeds, and also some weaker 238 day and 117 day periods; but these are probably related to Venus orbital characteristics, and in any case, are not very close

to the 150 day period presented in this paper. We note that the 150 day period is approximately 2/3 of the Venus sidereal orbital period. Perhaps the periodic variations seen in the clouds are an indication of a 3:2 resonance between the meridional Hadley-like circulation and solar influences (such as solar tides).

Looking toward microphysical phenomena, we compare the observed periodicity to the sedimentation and eddy diffusion (or, effectively, convective) timescales in the clouds. We noted previously that the Carlson et al. (1993) size parameter does not indicate an oscillation at the period exhibited by the 1.74 µm and 2.30 µm radiances, consistent with the findings of Barstow (2012). This behavior suggests that large scale changes in the ratio of the number of Mode 3 particles to the number of Mode 2′ particles are not responsible for the radiance variations observed. Now, there is sufficient variation in the calculated size parameter over the course of the observations reported here that we cannot say with certainty that the size parameter does not change at all during the course of the oscillation in the radiances. But we can say that if changes in the size parameter were driving the radiance changes seen, then a 150 day period should have appeared in the size parameter periodogram.

That it does not can only mean that either 1) only Mode 3 particles are growing larger (and smaller) to drive the oscillation, or 2) both Mode 2′ and Mode 3 are increasing (and decreasing) in total number concentration at similar rates. For the remainder of the discussion in this paragraph, we invite the reader to please consult Figure 1a of Grinspoon et al. (1993). That figure shows the extinction coefficients of the four traditional modes of cloud particles generally used in radiative transfer analysis of the Venus atmosphere. Note that the extinction coefficient of the Mode 3 particles is essentially flat between 1.74 µm and 2.30 µm, while the extinction coefficient for each of the Mode 2 and Mode 2′ particle modes exhibits a strong gradient with increasing wavelength between these two spectral windows. Hence, the size parameter is most strongly affected by changes in the size of the Mode 2 (or Mode 2′) particles, or by changes in the relative numbers of the Mode 3 and Mode 2 (or Mode 2′) particles. But, it is less strongly affected by changes in the size of the Mode 3 particles. In the 2.30 µm radiance (cloud opacity) and the 1.74 µm radiance (cloud opacity), we observe parallel variations, while noting an absence of a parallel variation in the size parameter. A change in Mode 3 particle size alone will increase the opacity of the clouds, but will have minimal effect on the size parameter, since the effect of the change in opacity will be comparable at the two wavelengths. Thus, an increase in Mode 3 particle size, while the number remains constant, and while the Mode 2′ number and size remain constant would be consistent with the observations reported here. Similarly, if the numbers of Mode 2′ and Mode 3 particles increase in a comparable manner (the more traditional interpretation of the size parameter), then we would expect an increase in opacity with a relatively unchanged size parameter.

If both modes of particles are considered to be sulfuric acid, then simple growth and evaporation mechanisms would suffice to explain changes in total particle number (option 2). But for one mode to increase in size while the other mode does not (option 1) would require either that the two modes have distinct compositions or that they are a single modal size distribution with a consistent composition that has been mistaken for two distinct populations, as Toon et al. (1984) have suggested. Furthermore, this would rule out coagulation processes as driving the observed variations, since this would preferentially increase the number of larger particles at the expense of the smaller particles. Of course, since coalescence time scales are so slow for the conditions in the condensational cloud (McGouldrick, 2007), it would be difficult to imagine them driving such variations.

Since the clouds that are the primary drivers of opacity differences at 1.74 µm are located between about 50 km and 57 km, we consider the timescales for particles to fall through such a 7 km distance. Furthermore, since the sedimentation can only remove particles from the clouds, we need another mechanism to resupply the cloud mass. So, we consider half the period to be the relevant timescale to compare to sedimentation processes. Thus, for a particle falling through the Venus atmosphere from an altitude of about 57 km to an altitude of about 50 km in a time of about 75 days, requires a sedimentation velocity of 0.11 cm/s. The gravitational sedimentation velocity of a droplet falling through a medium is given by Seinfeld and Pandis (1998) as:

$$v_{sed} = \frac{2}{9} \frac{r_p^2 \rho_p g C_c}{\mu} \qquad (6)$$

where $r_p$ is the radius of the particle, $\rho_p$ is its mass density (about $1.75\ g/cm^3$), $\mu$ is the viscosity of the medium (about $2 \times 10^{-4}\ \frac{g}{cm \cdot s}$ for this region of the Venus atmopshere), and $C_c$ is the unitless "Cunningham slip-correction factor," which for a 0.1µm particles is about 3, is about 1.2 for a 1µm radius particle, and asymptotes to 1.0 for particles with radius larger than ~3µm. The sedimentation velocity for a typical Mode 3 particle (3.65µm) under these consitions is 0.23 cm/s, while that of a Mode 2′ particle having a 1.4 µm radius is 0.041 cm/s, and of a Mode 2 particle with a 1.0 µm radius is 0.021 cm/s. For a gravitational sedimentation velocity of 0.11 cm/s, and expecting a particle radius near 1µm, consistent with previous in situ and remote measurements of the Venus clouds {Knollenberg and Hunten, 1980, Eq. 6 can be solved to find a particle size, $r_p = 2.2 \mu m$. If instead, we allow for very large particles (typical of Mode 3 and larger) by using a slip correction factor of 1.0, then we find a typical particle size of $r_p = 2.4 \mu m$. This is located between the sizes of the Mode 2′ and the Mode 3 particles generally considered to exist in the Venus condensational clouds. Hence, it is plausible that the clearing of the clouds (the increase in radiance) is consistent with rainout of the typically $1 - 3\ \mu m$-sized droplets in the Venus condensational clouds. If we consider instead a 10 km thick layer through which the particles must fall – which is plausible since a 47 km cloud base is not unreasonable, based on other analyses (Barstow et al., 2012) – then we find a typical particle size of $2.6 - 2.8 \mu m$, which is even closer to the Mode 3 population. However, if the Mode 3 particles are simply a large-radius tail of the Knollenberg and Hunten (1980) Mode 2, as suggested by Toon et al. (1984), then the typical modal radius of Mode 2′ would be pulled to larger values, possibly consistent with these calculations. In fact, these calculated modal radii would equate to effective radii (i.e., area-averaged radii) of between 2.8µm and 3.7µm, a range that includes the effective radii found in microphysics simulations of the condensational cloud driven by radiative-dynamical feedback (McGouldrick, 2016; McGouldrick and Toon, 2007). Note also that changes in the typical radius of cloud particles in the range from 2.2µm to 2.8µm will have minimal effect on the Carlson et al. (1993) size parameter in most cases, since the Mie scattering spectrum would more closely resemble Mode 3 than Mode 2′ at these radii, and hence would lie in a relatively flat part of the Mie scattering spectrum, according to previous work by Grinspoon et al. (1993), cf.their Figure 1a.

If we next consider the particle lifetime being driven by the eddy diffusion time scale, $(\Delta z)^2 / \kappa_{diff}$, then we find that a typical eddy diffusion coefficient of $\kappa_{diff} = 8\ m^2/s$ is required to fully mix a 10 km thick region within the 75 day observed timescale, while an eddy diffusion coefficient of 15 $m^2/s$ is required to fully mix a 7 km layer. Each of these also are consistent with the time-averaged eddy diffusion coefficients that were obtained from the radiative-dynamical simulations by McGouldrick and Toon (2007).

Finally, the radiative time constant for cooling from the altitude of the condensational clouds of Venus can be calculated as

$$\tau_{rad} = \frac{c_p \frac{P}{g} T_{mean}}{F}, \tag{7}$$

where $P/g$ is the total atmospheric column mass above the altitude in question (in this case, the condensational cloud tops at about 50 kPa), $c_p \sim 800 J/kg/K$ is the specific heat capacity of the Venus atmosphere averaged across that layer, $T_{mean} \sim 230$ K is the mean temperature above the cloud tops, and $F = 157$ W/m$^2$ is the emitted flux. The values of the atmospheric values listed above are calculated from the standard Venus International Reference Atmosphere (Seiff et al., 1985). The emitted flux is calculated by assuming that Venus has a Bond albedo of 0.76 (Moroz et al., 1985) and that the globally averaged emitted flux exactly balances the globally averaged incident solar flux. Performing this calculation, we find a radiative cooling time scale of about 76 days, almost exactly half the observed periodicity. Combining this with the eddy diffusional time scale above (which was driven by radiative heating of cloud base and cooling from the condensational cloud tops), we suggest that the 150 day period we see in the 1.74 µm mid-latitude radiance measured by VIRTIS-M on *Venus Express* is sustained by an interaction between radiative cooling and microphysical cloud processes, similar to those demonstrated by McGouldrick and Toon (2007).

Please note that, since the tendencies plotted here are averaged over large areas and times, and since the known spatial and temporal variability in the Venus condensational clouds is very large, it will be necessary to explore these relationships on shorter timescales; work that we are preparing for a future paper.

## 5. Conclusions

We have presented analysis of the complete *Venus Express* VIRTIS-M-IR data set for night side thermal emission in the near infrared spectral windows for all southern hemisphere observations made before the failure of the instrument's cooling system after orbit 921 (2008 October 27). We find no clear evidence of global long-term increase or decrease in the overall radiance (hence overall cloud coverage and thickness) from analysis of just the 1.74 µm and 2.30 µm spectral windows that are most sensitive to the cloud variations. However, at mid-latitudes, the radiance steadily increases through the duration of the VIRTIS-M-IR lifetime, while steadily decreasing with time near the poles. This may be an indication of a transfer of cloud mass poleward, an inhibiting of heat transfer by the meridional circulation, or subtle vertical or meridional wanderings of the meridional circulation cell. This long-term radiance trend might represent a manifestation of heat energy transport in parallel with the momentum transport indicated by the variations in zonal wind speeds previously inferred from cloud tracking studies.

Our global analysis of the Carlson et al. (1993) size parameter demonstrates an overall increase in size parameter, hence particle size, from equator to pole, consistent with previous particular analysis by Wilson et al. (2008). We also note a subtle increase in the size parameter peaking at about $-20°$ latitude; but it is difficult to state its existence with certainty, due to the increasing magnitude of the standard deviation of the calculated size parameter in the equatorial latitudes observed by VIRTIS-M-IR, possibly amplified by instrumental artifacts.

We observe in the VIRTIS-M-IR data that the 1.74 µm and 2.30 µm windows demonstrate local maxima in radiance peaking around 50° latitude, consistent with previous observations of these spectral windows, dating to the time of their discovery in the1980's. We also measure a large amount of variability to the typical cloud coverage as at latitudes between 0° and 60°, as ev-

idenced by the very large standard deviations about the mean in the cloud-dominated windows at those latitudes.

Finally, we report the existence of a roughly 150-day periodic variation in the cloud coverage, seen most prominently at mid-latitudes in the 1.74 µm radiance data. A least squares frequency analysis quantifies this period that was suggested in earlier work by McGouldrick et al. (2012). The timescale is consistent with a cloud formation and evolution cycle that is driven by the radiative dynamical feedback and gravitational settling of particles with sizes typical of the condensational clouds. Further modeling investigations will be necessary to elucidate the drivers of this periodicity in the clouds.

## References

Allen, D.A., Crawford, J.W., 1984. Cloud structure on the dark side of Venus. Nature 307, 222–224. doi:10.1038/307222a0.

Barstow, J.K., 2012. Global Cloud Properties on Venus from Orbital Infrared Spectroscopy. University of Oxford Ph.d. thesis.

Barstow, J.K., Tsang, C.C.C., Wilson, C.F., Irwin, P.G.J., Taylor, F.W., McGouldrick, K., Drossart, P., Piccioni, G., Tellmann, S., 2012. Models of the global cloud structure on Venus derived from Venus Express observations. Icarus 217, 542–560. doi:10.1016/j.icarus.2011.05.018.

Bézard, B., Tsang, C.C.C., Carlson, R.W., Piccioni, G., Marcq, E., Drossart, P., 2009. Water vapor abundance near the surface of Venus from Venus Express/VIRTIS observations. J. Geophys. Res. 114, E00B39. doi:10.1029/2008JE003251.

Bravo, J.P., Roque, S., Estrela, R., Leão, I.C., DeMedeiros, J.R., 2014. Wavelets: a powerful tool for studying rotation, activity, and pulsation in Kepler and CoRoT stellar light curves. Astron. Astrophys. 568, A34. doi:10.1051/0004-6361/201323032.

Bullock, M.A., Grinspoon, D.H., 2001. The recent evolution of climate on Venus. Icarus 150, 19–37. doi:10.1006/icar.2000.6570.

Carlson, R.W., Kamp, L.W., Baines, K.H., Pollack, J.B., Grinspoon, D.H., Encrenaz, T., Drossart, P., Taylor, F.W., 1993. Variations in Venus cloud particle properties: a new view of Venus's cloud morphology as observed by Galileo Near-infrared Mapping Spectrometer. Planet. Space Sci. 41, 477–485. doi:10.1016/0032-0633(93)90030-6.

Chanover, N.J., Glenar, D.A., Hillman, J.J., 1998. Multispectral near-IR imaging of Venus nightside cloud features. J. Geophys. Res. 103, 31335–31348. doi:10.1029/1998JE900009.

Crisp, D., Sinton, W.M., Hodapp, K.W., Ragent, B., Gerbault, F., Goebel, J.H., Probst, R.G., Allen, D.A., Pierce, K., Stapelfeldt, K.R., 1989. The nature of the near-infrared features on the Venus night side. Science 246, 506–509. doi:10.1126/science.246.4929.506.

Drossart, P., Piccioni, G., Adriani, A., Angrilli, F., Arnold, G., Baines, K., Bellucci, G., Benkhoff, J., Bézard, B., Bibring, J., Blanco, A., Blecka, M., Carlson, R., Coradini, A., Di Lellis, A., Encrenaz, T., Erard, S., Fonti, S., Formisano, V., Fouchet, T., Garcia, R., Haus, R., Helbert, J., Ignatiev, N., Irwin, P., Langevin, Y., Lebonnois, S., Lopez-Valverde, M., Luz, D., Marinangeli, L., Orofino, V., Rodin, A., Roos-Serote, M., Saggin, B., Sanchez-Lavega, A., Stam, D., Taylor, F., Titov, D., Visconti, G., Zambelli, M., Hueso, R., Tsang, C., Wilson, C., Afanasenk, T., 2007. Scientific goals for the observation of Venus by VIRTIS on ESA/Venus Express mission. Planet. Space Sci. 55, 1653–1672. doi:10.1016/j.pss.2007.01.003.

Esposito, L.W., Copley, M., Eckert, R., Gates, L., Stewart, A.I.F., Worden, H., 1988. Sulfur dioxide at the Venus cloud tops, 1978–1986. J. Geophys. Res. 93, 5267–5276. doi:10.1029/JD093iD05p05267.

Grinspoon, D.H., Pollack, J.B., Sitton, B.R., Carlson, R.W., Kamp, L.W., Baines, K.H., Encrenaz, T., Taylor, F.W., 1993. Probing Venus's cloud structure with Galileo NIMS. Planet. Space Sci. 50, 515–542. doi:10.1016/0032-0633(93)90034-Y.

Haus, R., Kappel, D., Arnold, G., 2014. Atmospheric thermal structure and cloud features in the southern hemisphere of Venus as retrieved from VIRTIS/VEX radiation measurements. Icarus 232, 232–248. doi:10.1016/j.icarus.2014.01.020.

Hueso, R., Peralta, J., Garate-Lopez, I., Bandos, T.V., Sánchez-Lavega, A., 2015. Six years of Venus winds at the upper cloud level from UV, visible and near infrared observations from VIRTIS on Venus Express. Planet. Space Sci. 113, 78–99. doi:10.1016/j.pss.2014.12.010.

Hueso, R., Peralta, J., Sánchez-Lavega, A., 2012. Assessing the long-term variability of Venus winds at cloud level from VIRTIS-Venus Express. Icarus 217, 585–598. doi:10.1016/j.icarus.2011.04.020.

Imamura, T., Hashimoto, G.L., 1998. Venus cloud formation in the meridional circulation. J. Geophys. Res. 103, 31349–31366. doi:10.1029/1998JE90010.

Kamp, L.W., Taylor, F.W., Calcutt, S.B., 1988. Structure of Venus's atmosphere from modelling of night-side infrared spectra. Nature 336, 360–362. doi:10.1038/336360a0.

Kappel, D., Arnold, G., Haus, R., Piccioni, G., Drossart, P., 2012. Refinements in the data analysis of VIRTIS-M-IR Venus nightside spectra. Adv. Space Res. 50, 228–255. doi:10.1016/j.asr.2012.03.029.

Khatuntsev, I.V., Patsaeva, M.V., Titov, D.V., Ignatiev, N.I., Turin, A.V., Limaye, S.S., Markiewicz, W.J., Almeida, M., Roatsch, T., Moissl, R., 2013. Cloud level winds from the Venus express monitoring camera imaging. Icarus 226, 140–158. doi:10.1016/j.icarus.2013.05.018.

Knollenberg, R.G., Hunten, D.H., 1980. The microphysics of the clouds of Venus: results of the pioneer Venus particle size spectrometer experiment. J. Geophys. Res. 85, 8038–8058. doi:10.1029/JA085iA13p08039.

Kouyama, T., Imamura, T., Nakamura, M., Satoh, T., Futaana, Y., 2013. Long-term variation in the cloud-tracked zonal velocities at the cloud top of Venus deduced from Venus Express VMC images. J. Geophys. Res. 118, 37–46. doi:10.1029/2011JE004013.

Lebonnois, S., Covey, C., Grossman, A., Parish, H., Schubert, G., Walterschied, R., Lauritzen, P., Jablonowski, C., 2012. Angular momentum budget in General Circulation Models of superrotating atmospheres: a critical diagnostic. J. Geophys. Res. 117, E12004. doi:10.1029/2012JE004223.

Lomb, N.R., 1976. Least-squares frequency analysis of unequally spaced data. Astrophys. Space Sci. 39, 447–462. doi:10.1007/BF00648343.

Longobardo, A., Palomba, E., Zinzi, A., Piccioni, G., Tsang, C.C.C., Drossart, P., 2012. Limb darkening study using Venus nightside infrared spectra from VIRTIS-Venus express data. Planet. Space Sci. 69, 62–75. doi:10.1016/j.pss.2012.04.004.

Marcq, E., Bertaux, J.L., Montmessin, F., Belyaev, D., 2012. Variations of sulfur dioxide at the cloud top of Venus's dynamic atmosphere. Nature Geosci. 6, 25–28. doi:10.1038/ngeo1650.

Marcq, E., Bézard, B., Encrenaz, T., Birlan, M., 2005. Latitudinal variations of CO and OCS in the lower atmosphere of Venus from near-infrared nightside spectro-imaging. Icarus 179, 375–386. doi:10.1016/j.icarus.2005.06.018.

McGouldrick, K., 2007. Microphysics and Radiative-Dynamical Feedback in the Near Infrared Brightness Features in the Venus Clouds. University of Colorado Ph.d. thesis.

McGouldrick, K., 2016. Influence of coagulation on Venus cloud microphysics. In Preparation.

McGouldrick, K., Baines, K.H., Momary, T.W., Grinspoon, D.H., 2008. Venus Express / VIRTIS observations of middle and lower cloud variability and implications for dynamics. J. Geophys. Res. 113, E00B14. doi:10.1029/2008JE003113.

McGouldrick, K., Momary, T.W., Baines, K.H., Grinspoon, D.H., 2012. Quantification of middle and lower cloud variability and mesoscale dynamics from Venus Express/VIRTIS observations at 1.74μm. Icarus 217, 615–628. doi:10.1016/j.icarus.2011.07.009.

McGouldrick, K., Toon, O.B., 2007. Investigation of possible causes of the holes in the condensational Venus cloud using a microphysical cloud model with a radiative-dynamical feedback. Icarus 191, 1–24. doi:10.1016/j.icarus.2007.04.007.

Moinelo, A.C., Piccioni, G., Ammannito, E., Filacchione, G., Drossart, P., 2010. Calibration of hyperspectral imaging data: VIRTIS-M onboard Venus Express. IEEE Trans. Geosci. Rem. Sens. 48, 3941–3950. doi:10.1109/TGRS.2010.2064325.

Moroz, V.I., Ékonomov, A.P., Moshkin, B.E., Revercomb, R.H., Sromovsky, L.A., Schofield, J.T., 1985. Solar and thermal radiation in the Venus atmosphere. Adv. Space Res. 5, 197–232. doi:10.1016/0273-1177(85)90202-9.

Mueller, N., Helbert, J., Hashimoto, G.L., Tsang, C.C.C., Erard, S., Piccioni, G., Drossart, P., 2008. Venus surface thermal emission at 1 µm in VIRTIS imaging observations: Evidence for variation of crust and mantle differentiation conditions. J. Geophys. Res. 113, E00B17. doi:10.1029/2008JE003118.

Nakamura, M., Imamura, T., Ishii, N., Abe, T., Kawakatsu, Y., Hirose, C., Satoh, T., Suzuki, M., Ueno, M., Yamazaki, A., Iwagami, N., Watanabe, S., Taguchi, M., Fukuhara, T., Takahashi, Y., Yamada, M., Imai, M., Ohtsuki, S., Uemizu, K., Hashimoto, G.L., Takagi, M., Matsuda, Y., Ogohara, K., Sato, N., Kasaba, Y., Kouyama, T., Hirata, N., Nakamura, R., Yamamoto, Y., Horinouchi, T., Yamamoto, H., Hayashi, Y., Kashimura, H., Sugiyama, K., Sakanoi, T., Ando, H., Murakami, S., Sato, T.M., Takagi, S., Nakajima, K., Peralta, J., Lee, Y.J., Nakatsuka, J., Ichikawa, T., Inoue, K., Toda, T., Toyota, H., Tachikawa, S., Narita, S., Hayashiyama, T., Hasegawa, A., Kamata, Y., 2016. AKATSUKI returns to venus. Earth, Planets Space 68, 75. doi:10.1186/s40623-016-0457-6.

Nakamura, M., Imamura, T., Ueno, M., Iwagami, N., Satoh, T., Watanabe, S., Taguchi, M., Takahashi, Y., Suzuki, M., Abe, T., Hashimoto, G.L., Sakanoi, T., Okano, S., Kasaba, Y., Yoshida, J., Yamada, M., Ishii, N., Yamada, T., Uemizu, K., Fukuhara, T., Oyama, K., 2007. Planet-C: Venus Climate Orbiter mission of Japan. Planet. Space Sci. 55, 1831–1842. doi:10.1016/j.pss.2007.01.009.

Parish, H.F., Schubert, G., Covey, C., Walterscheid, R.L., Grossman, A., Lebonnois, S., 2011. Decadal variations in a Venus general circulation model. Icarus 212, 42–65. doi:10.1016/j.icarus.2010.11.015.

Scargle, J.D., 1982. Studies in astronomical time series analysis. II. Statistical aspects of spectral analysis of unevenly spaced data. Astrophys. J. 263, 835–853. doi:10.1086/160554.

Seiff, A., Schofield, J.T., Kliore, A.J., Taylor, F.W., Limaye, S.S., Revercomb, H.E., Sromovsky, L.A., Kerzhanovich, V.V., Moroz, V.I., Marov, M.Y., 1985. Models of the structure of the atmosphere of Venus from the surface to 100 km altitude. Adv. Space Res. 5, 3–58. doi:10.1016/0273-1177(85)90197-8.

Seinfeld, J.H., Pandis, S.N., 1998. Atmospheric Chemistry and Physics. John Wiley & Sons, Inc., New York.

Shalygin, E.V., Markiewicz, W.J., Basilevsky, A.T., Titov, D.V., Ignatiev, N.I., Head, J.W., 2015. Active volcanism on Venus in the Ganiki Chasma rift zone. Geophys. Res. Lett. 42, 4762–4769. doi:10.1002/2015GL064088.

Toon, O.B., Ragent, B., Colbourn, D., Blamont, J., Cot, C., 1984. Large, solid particles in the clouds of Venus: do they exist? Icarus 57, 143–160. doi:10.1016/0019-1035(84)90063-0.

Wilson, C.F., Guerlet, S., Irwin, P., Tsang, C.C.C., Taylor, F.W., Carlson, R.W., Drossart, P., Piccioni, G., 2008. Evidence for anomalous cloud particles at the poles of Venus. J. Geophys. Res. 113, E00B13. doi:10.1029/2008/JE003108.